Check for updates

Metal–organic framework and graphene composites: advanced materials for electrochemical supercapacitor applications

Debal Kanti Singha, [ID] [a] Rupali Ipsita Mohanty, [ID] [ab] Piyali Bhanja [ID] [a] and Bikash Kumar Jena [ID] *[ab]

Metal–organic frameworks (MOFs) with diverse, periodical structures bearing high surface area and tunable pore size have appeared as a new porous hybrid advanced class of material constructed from organic linkers and metal-containing nodes. Due to their high porosity and thermal and mechanical stability, they can be applied in different noteworthy applications. The low conductivity property of MOFs generates a problem for their supercapacitor applications. Thus, their composite formation with graphene can overcome the drawbacks of MOFs and benefit from two-parent constituents. In this context, we give a brief introduction to supercapacitors made from MOF-based graphene composites. Different kinds of supercapacitor with their working principles are also discussed here. This review article focuses on the development of functionalized MOF-based graphene composites by adopting various synthetic strategies and their application in energy storage supercapacitors. The benefits of MOF–graphene composites in supercapacitor applications are also discussed here.

[a] Materials Chemistry Department, CSIR-Institute of Minerals and Materials Technology, Bhubaneswar, Odisha, 751013, India. E-mail: bikash@immt.res.in
[b] Academy of Scientific & Innovative Research, Ghaziabad, 201002, India

1 Introduction

In this era, the limitations of renewable energy resources and the lack of fossil fuel energy are playing a crucial part in developing clean and sustainable energy sources in

Debal Kanti Singha

Dr Debal Kanti Singha received his BSc degree in Chemistry from Bankura Christian College (under The University of Burdwan) in 2011. He completed his MSc degree in 2013 from Visva-Bharati University. He obtained his PhD in Chemistry from Visva-Bharati University under the joint supervision of Dr Sudip Kumar Mondal of Visva-Bharati University and Dr Partha Mahata of Jadavpur University. Currently he is working as a Post-Doctoral Researcher (Senior Project Associate) at CSIR-Institute of Minerals and Materials Technology under the guidance of Dr Bikash Kumar Jena. His current research interests are focused on the areas of supercapacitors, electrocatalysis, and sensing using nanomaterials and MOFs.

Rupali Ipsita Mohanty

Rupali Ipsita Mohanty graduated in Chemistry honours from Utkal University, Odisha in 2016. After that, she completed her Master's in Chemistry from the College of Engineering and Technology in 2018. In addition to that, she had an internship in electrocatalysis at the School of Chemical Sciences, NISER. Currently, she is pursuing her PhD under the supervision of Dr Bikash Kumar Jena at CSIR-Institute of Minerals and Materials Technology, Bhubaneswar, Odisha. Her area of study is focused on the development of porous metal phosphonates for electrochemical energy conversion and storage applications.

economically advanced ways.[1–3] CO_2 emission during the process generates an environmental problem. To solve these problems, extensive research is going on all over the globe, concentrating on clean, sustainable, and renewable energy resources that can replace fossil fuels.[4,5] In this regard, solar energy, tidal energy, and wind energy have been considered as alternatives.[6] But these energy sources are not available for an uninterrupted time or they depend on the time of day or location.[7–10] Energy storage and conversion devices have become very important to the scientific community. Besides with the rapid development in means of transportation, such as fully electric vehicles, plug-in hybrids, and hybrid electric vehicles, and consumer electronics extending from laptops, to digital cameras, mobile phones, and emergency doors, the requirements for the power and energy density of energy storage devices have increased.[11–14] The battery is the most frequently used energy storage device. High energy capacity batteries can be applied in many fields.[15] But the lower power density of a battery provides a barrier to its application that requires a large power impulse. Supercapacitors can provide high power density and specific capacitance, a longer cycle life, a faster charge–discharge rate, excellent reversibility, a wide thermal operating range, cost-effectiveness, and self-operation in devices, all of which make supercapacitors an active area of research.[16–29] These characteristics of supercapacitors are extensively used in gadgets such as electronic equipment, camera flashes, digital communication devices, by the military, in aerospace, as industrial accessories, *etc.*[30–38] Supercapacitors comprise four main components: electrode materials, a current collector, electrolyte, and a separator.[39] The ion permeability of the separator permits ionic charge transfer. Supercapacitors

with high power densities, moderate energy density, and long cycle stability bridge the gap between traditional capacitors and batteries.[40–45] The lower energy density of supercapacitors, compared with batteries and fuel cells, creates a challenge at this current time.[46,47] So, researchers are motivated on a determined pathway to enhance the absolute energy of supercapacitors through the development of new electrodes and electrolytes, and through innovative device fabrication.[48,49] However, a supercapacitor depends on two charge storage mechanisms: *i.e.*, EDLCs and pseudocapacitors. In EDLCs, charge species are adsorbed onto the surface of the electrode. In contrast, in pseudocapacitors, intercalation of ion species occurs between the electrode and electrolyte interface, resulting in the faradaic redox reaction of the active materials.

Different kinds of materials, including metal oxides, metal phosphides, graphene derivatives, covalent–organic frameworks (COFs), MOFs, and porous carbon materials, have been reported for their application in supercapacitors.[7,50–66] In 1995, Yaghi and co-workers discovered MOFs, and since then MOFs have been widely used in various applications.[67] This term became more popular when Yaghi and coworkers discovered the structure of MOF-5.[68] MOFs built by connecting organic ligands with metal clusters, or metal ions[69–73] made a bright appearance in the area of hybrid crystalline substances. The choice of metal ions or metal clusters with an appropriate organic ligand structure allows the formation of MOFs in different dimensions.[37] Compared to other porous materials, the pore size of the framework could be easily controlled by altering the length of the organic linker. MOFs with tunable pore structures, redox-active metal centres, and large surface areas are bright candidates for electrode materials for

Dr Piyali Bhanja graduated from Jadavpur University (India) in 2011 and gained a Masters from the Indian Institute of Technology, Madras in 2013. She has received her PhD in 2018 from the Indian Association for the Cultivation of Science, Kolkata. During her PhD she was a part-time intern in the INDO-UK project of DST-UKIERI at University of Central Lancashire, UK. Then, she was a JSPS postdoctoral fellow at the

Piyali Bhanja

National Institute for Materials Science, Japan. Currently, she is working in CSIR-Institute of Minerals and Materials Technology, India as a Ramanujan fellow. Her research field is nanoscale porosity in metal phosphate/phosphonates and polymers, and their electrochemical energy conversion and storage applications.

Dr Bikash Kumar Jena, FRSC is presently working as a Senior Principal Scientist for CSIR-Institute of Minerals and Materials Technology, India. He received his PhD from the IIT Kharagpur, India and postdoc at UW, USA and TUM, Germany. His scientific interests are on materials chemistry, Electrocatalysis (HER/OER/ORR/NRR/ CO_2RR) Energy storage (supercapacitor/Metal air batteries), sensing, etc. His con-

Bikash Kumar Jena

tributions earned recognition (young scientist awards) from the National Academy of Sciences India (NASI), CSIR, Indian Science Congress Association, Indian Society of Electroanalytical Chemistry, Odisha Bigyan Academy; he was awarded a CRSI Bronze Medal, and is a Fellow of the Royal Society of Chemistry, London UK. He has published more than 94 papers in international journals ((> 5400 citations, H index: 38) and filed more than 7 patents.

supercapacitor applications.[74,75] But their low conductivity property generates a problem for supercapacitor applications.[76,77] However, the synergistic effect of bimetallic MOFs provides enhanced supercapacitor performance compared to monometallic MOFs. On the other hand, graphene has a large theoretical surface area, good electrochemical stability, high conductivity, and other distinct chemical and physical properties that have gathered significant attention for supercapacitor applications. The number of individual articles reported for supercapacitor applications in the last few years, expressly since 2018, using MOF and graphene, is provided in Fig. 1(a). The formation of a composite with graphene can overcome the drawbacks of MOFs and benefit from two-parent constituents. Combining hetero-structured MOFs with graphene enhances the electrical conductivity of the matrix, which is helpful for faster ionic movement in electrochemical reactions. Due to this, the interfacial interaction can be improved, ensuring faster charge storage kinetics. Also, the durability of the composite could be improved by integrating MOFs with

graphene because of the increased contact area with the electrolytic ions. Agglomeration of graphitic layers in graphene oxide can be diminished by a composite with MOFs, resulting in a higher electro-active surface area in the materials. For these reasons, a few review articles have been published based on MOF–graphene composites, focusing on their synthesis and their potential applications for different purposes.[78–84] But in the above-mentioned review articles, multiple applications of MOF–graphene composites are described. In this review article, we present a focused and updated discussion about the application of MOF–graphene composites in electrochemical supercapacitor applications. Measurement of the electrochemical performance of supercapacitors, types of supercapacitors, and materials for supercapacitors are discussed in this review article. We discuss the MOF–graphene composites thoroughly based on different metal-based MOF–graphene composites. The benefits of MOF–graphene composites in supercapacitor applications are also discussed with proper explanation in this section. We also give an idea of various other MOF-based
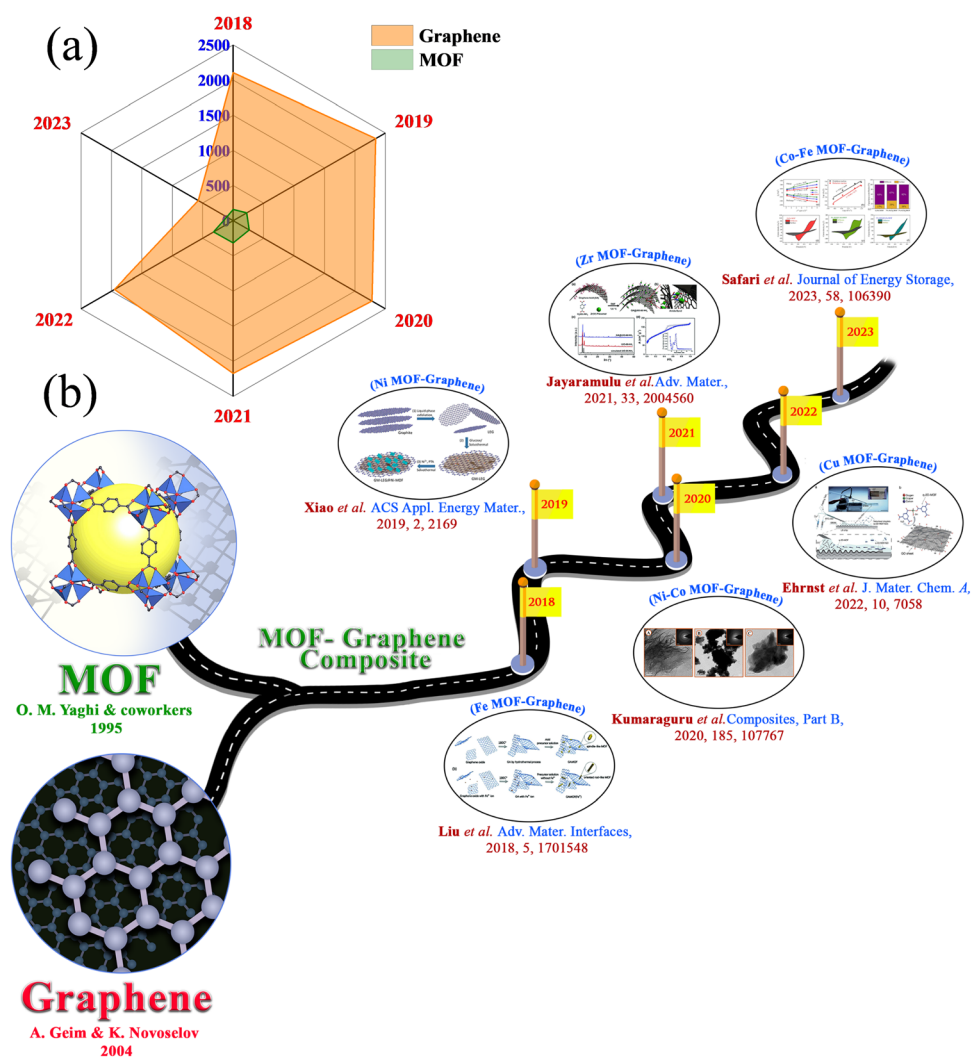

Fig. 1 (a) Radar plot showing the number of journal publications on MOF and graphene for supercapacitor application since 2018 (source: ISI Web of Knowledge). (b) The timeline displays recent progress in the development of different MOF–graphene composites.

composites and their derivatives for supercapacitor applications. Different types of MOF–graphene composites have flourished over time, and their supercapacitor applications have been explored (Fig. 1(b)).

2 Electrochemical performance measurement of supercapacitor electrode materials

The supercapacitor performance of an as-obtained electrode has been evaluated by performing various electrochemical measurements like cyclic voltammetry (CV), galvanostatic charge–discharge (GCD), and electrochemical impedance spectroscopy (EIS). One can obtain the values of basic parameters like current, voltage, and time from the above measures. From the values of the above parameters, it is possible to obtain the values of other related parameters, including specific capacitance, cyclic stability, energy density, power density, and charge transfer resistance of the supercapacitor. These parameters are essential for the supercapacitance performance of the electrode materials. From cyclic voltammetry, the specific capacitance (C) of an electrode could be calculated using the equation:

$$C(\text{F g}^{-1}) = \frac{\int_{V_1}^{V_2} I(V)\mathrm{d}V}{m\nu(V_2 - V_1)}$$

where C is the specific capacitance (in F g^{-1}), m is the mass of the active electrode (in g), ν is the scan rate (in Vs^{-1}), V_1 and V_2 are the potential limits (in V) and $\int_{V_1}^{V_2} I(V)\mathrm{d}V$ indicates the area under the CV curve over an operational voltage range. The specific capacitance from the galvanostatic charge–discharge (GCD) analysis can be determined using the following equation:

$$C(\text{F g}^{-1}) = \frac{I \int V(t)\mathrm{d}t}{m(V_2 - V_1)}$$

where I indicates the steady discharge current applied (in A) for GCD measurement, m is the mass of the active electrode (in g), $\int V(t)\mathrm{d}t$ is the area under the discharge curve, and $(V_2 - V_1)$ is the working potential window (in V). The energy density (E) and the power density (P) of a supercapacitor can be calculated as:

$$E = \frac{1}{2 \times 3.6} C(V_2 - V_1)^2$$

and

$$P = \frac{3600E}{t}$$

3 Types of supercapacitor

Supercapacitors can be divided into three categories based on the pathway of energy storage: (i) electrical double-layer capacitors (EDLCs), (ii) pseudocapacitors, and (iii) hybrid
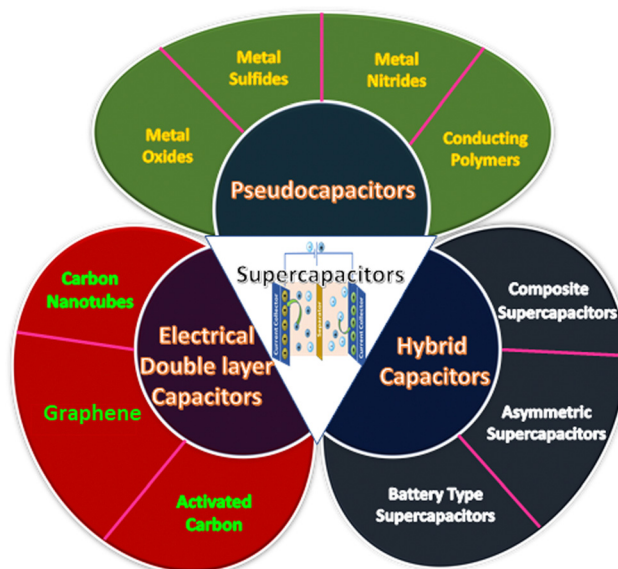

Fig. 2 Classification of supercapacitors.

capacitors. A classification of supercapacitors based on charge storage mechanism is provided in Fig. 2.

3.1 Electrical double-layer capacitors (EDLCs)

EDLCs are formed by the combination of two electrodes and an electrolyte. In EDLCs, charge storage is possible either electrostatically or through a non-faradaic process, which can be generated from the accumulation of the charges at the electrode–electrolyte interface. The electrical double layer is the principle behind energy storage in EDLCs. So, the pore size distribution and the accessible surface/interface features of the electrode materials generally determine the capacitance of EDLCs.[85] This charge separation allows the formation of the electrical double layer. In EDLCs, charge storage occurs through a surface phenomenon. EDLCs allow quick energy uptake, power performance, and energy delivery. Carbon-containing substances, such as graphene, activated carbon, or carbon nanotubes, are usually applied as electrode materials for EDLCs. These materials possess high conductivity, a large surface area, and high-temperature stability.[86] EDLCs possess higher power density as well as superb charge–discharge cycling stability, as the chemical reaction occurs at the electrode surface during the charge–discharge process.[85] But EDLCs have a relatively low energy density and limited specific capacitance.[87,88] Enhancing the conductivity and controlling the pore size and surface area are the most fruitful approaches to achieving high capacitance in an EDLC.[89,90]

3.2 Pseudocapacitors

In pseudocapacitors, a quick faradaic redox reaction of electroactive materials at the interface is involved where the charge transfer has occurred, which is the reason behind the energy storage. The larger specific capacitance and energy densities of pseudocapacitors compared to EDLCs are due to the involvement of the faradaic process. Usually, conducting polymers and

metal oxides, especially transition metal oxides, sulfides, selenides, and nitrides, are used as electrode materials for pseudocapacitors.

3.3 Hybrid capacitors

EDLCs exhibit good power performance and cyclic stability, whereas pseudocapacitors possess a high specific capacitance value. Hybrid capacitors are special supercapacitors that combine EDLCs (non-faradaic) and pseudocapacitors (faradaic).

3.3.1 Composite supercapacitors.
A composite supercapacitor is a combination of carbon-containing substances with conducting polymers or metal oxide frameworks. Here, the charge storage process is controlled by both chemical and physical processes. A carbon-based material with a high specific surface area provides an electrical double layer and greater contact between electrolyte and pseudocapacitive materials. On the other hand, the pseudocapacitive material enhances the capacitance of the composite electrode via a faradaic reaction.[91,92]

3.3.2 Asymmetric supercapacitors.
Asymmetric hybrid capacitors involve non-faradaic and faradaic processes. Coupling between EDLC and a pseudocapacitor electrode occurs. In an asymmetric supercapacitor, a conducting polymer or metal oxide is utilized as a positive electrode, while a carbon material is utilized as a negative electrode.[91,92]

3.3.3 Battery-type supercapacitors.
Combining a supercapacitor electrode with a battery-type material generates a battery-type supercapacitor. Here, the backdrop of a supercapacitor and batteries have been used to construct a set-up in one cell.[91,92]

4 Materials for supercapacitors

Different kinds of materials, including metal oxides, metal phosphides, graphene derivatives, COFs, MOFs, and porous carbon materials, have been reported for application in supercapacitors.[7,50–63]

4.1 Metal–organic frameworks (MOFs)

MOFs designed by connecting organic ligands with metal clusters, or metal ions[69–73] have made a bright appearance in the area of hybrid crystalline substances as highly encouraging materials with diverse structural characteristics and have found application for different purposes, such as gas storage, gas separation, magnetism, catalysis, sensing, or drug delivery, over the last two decades.[93–107] The interconnected pores within MOFs provide a distinctively confined environment where new physical and chemical properties can be developed. MOFs are generally synthesized via solvothermal techniques.[108–112] But mechanochemical methods,[113–116] electrochemical routes,[117–120] sonochemical routes,[121–124] microwave-assisted syntheses,[125–128] and slow-layer diffusion techniques[129–133] are also used for the preparation of MOFs. In MOFs, the pore size and surface area can be tuned by using suitable ligands as the linkers. There is a possibility of incorporating a particular group within the framework structure. The shape and size-controlled synthesis of MOFs at macro and nanoscales is also possible. In comparison with other porous materials, the pore size of the framework could be easily controlled by altering the length of the organic linker. MOFs can be deposited onto various substrates to obtain composites with other carbon-based supports to improve their conducting and electrical properties. MOFs can be assembled with graphene sheets to form composites after dispersing the nanosheets into the MOF parent solutions.[134,135] Many MOFs could be synthesized with different structures, as diverse choices of linker and metal are possible. Recently, their application has been reported for supercapacitor purposes.[74,75]

4.2 Graphene

Among all the most propitious allotropes of carbon, graphene has attracted massive attention in the nanomaterials field due to two distinctive properties: good electrical behaviour and an excellent robust structure.[136] On the other hand, graphene oxide can be synthesized easily from graphite mesh, and is a graphene congener with countless oxygen-bearing functionalities, which allows the construction of a broad spectrum of new functional groups.[137] Also, the nanostructure of graphene oxide is made off the basal plane, which is enriched with epoxy, hydroxyl, and carboxylic acid functional groups. Due to the unique structure of carbon containing one-atom-thick layers arranged in a honeycomb unit, graphene oxide can be used as a building block to efficiently synthesize 2D porous hybrid nanomaterials. Recently, graphene has been selected as an encouraging carbon-based material with huge possibilities in the industrial field to favour different catalytic organic transformation reactions such as hydration of alkenes,[138] oxidation of thiols,[139] and aerobic oxidation of alcohols, which can be converted into the associated aldehydes and ketones.[140] However, it is relevant to state that graphene oxide is hydrophilic due to the existence of a broad range of oxygen-bearing groups on the basal planes and edges, which can facilitate the grafting of the active metal ions onto the surface. Optimization followed by standardization of the chemical reaction and the development of an environmentally-friendly chemical reaction can be successfully performed via the participation of a porous material containing suitable organic groups inside the pore wall, which can provide fascinating technological and energy-related improvements.

4.3 MOF–graphene composites

In the case of MOF, the vital role of the metal ion is to form the backbone of the framework in supercapacitor applications. Different metal-based MOFs are reported to be used to prepare MOF–graphene composites, which are superior to pure MOF and graphene. The benefits are as follows: (i) the aggregation of two substances could be interrupted owing to the inclusion of graphene-based materials; (ii) high electrical conductivity could be maintained over the electrode; (iii) the cycling stability of the electrode could be increased at the time of the charge–discharge process; and (iv) the structural feature of the
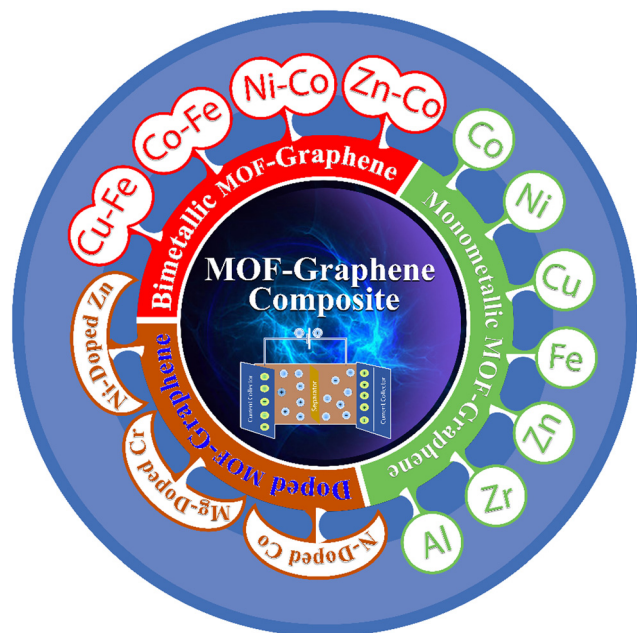
Fig. 3 Schematic presentation of different metal-ion-based MOF–graphene composites for supercapacitor applications.
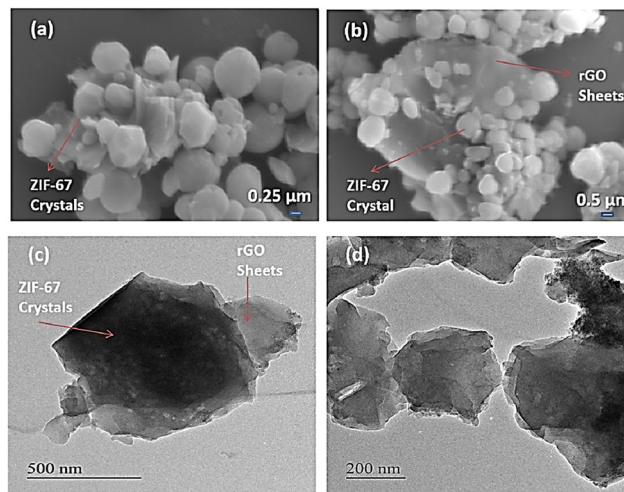

Fig. 4 FESEM images of (a) ZIF-67 and (b) ZIF-67/rGO. (c) and (d) TEM images of the ZIF-67/rGO composite. Reproduced from ref. 141 with permission from American Chemical Society, Copyright 2018.

pseudocapacitive material could remain unaltered and inhibit detachment from the graphene surface at the time of the charge–discharge process. Here, we discuss the supercapacitor application of MOF–graphene composites based on the different metal ions involved in building the MOF structure (see the detailed illustration in Fig. 3).

4.3.1 Co-based MOF–graphene composites. Sundriyal *et al.* used a simple stirring method to synthesize a ZIF-67 and reduced graphene oxide composite.[141] The composite showed all the diffraction patterns of the MOF besides the low-intensity 2θ peak at 25.6° (002) of reduced graphene oxide (rGO) in XRD analysis. This confirmed the successful incorporation of the ZIF into the composite. The SEM analysis confirmed the apparent growth of the MOF crystals over the sheet-like surface of rGO (Fig. 4(a) and (b)). Composite formation between ZIF-67 and rGO was also evidenced from the TEM analysis, where the ZIF-67 crystal remains over the rGO sheet (see Fig. 4(c) and (d)). EDX analysis was performed to confirm the presence of cobalt, carbon, oxygen, and nitrogen in the composite. The Raman spectra of the composite showed peaks at 1349 and 1579 cm^{-1} due to the D and G bands of the rGO nanosheet, respectively. Peaks observed at 262, 424, 521, and 681 cm^{-1} suggested the presence of ZIF-67 in the composite. FTIR spectra of the composite exhibited a strong band at 1662 cm^{-1}, confirming the presence of epoxide, which arises from the reduction of GO to rGO. The presence of ZIF-67 is confirmed by the appearance of bands at 1580, 1428, 1304, 1142, 996, and 759 cm^{-1}. The specific surface area obtained from the N$_2$ adsorption–desorption isotherm of the composite is 571 m^2 g^{-1}. The supercapacitor performance of the composite was checked in a mixture of 0.2 M K$_3$[Fe(CN)$_6$] and 1 M Na$_2$SO$_4$. The composite material has a high specific surface area, good conductivity,

and low resistance, favouring its application in supercapacitors. Three-electrode systems were used for the measurement of supercapacitor performance. At a current density of 4.5 A g^{-1}, the obtained specific capacitance value was 1453 F g^{-1} with 90% capacity retention after 1000 continuous cycles. They also assembled a two-electrode symmetrical electrode using ZIF-67/rGO electrodes. The operation of the symmetrical supercapacitor in redox additive electrolyte (RAE) delivered a specific capacitance of 326 F g^{-1} at a current density of 3 A g^{-1}. After performing 1000 charge–discharge cycles, the device retained $\sim$88.8% specific capacitance, indicating good cyclic stability. A white LED was illuminated for at least 3 minutes using a series of two symmetrical devices for practical application.

Wang and co-workers synthesized nanocubes of ZIF-67 by mixing 2-methyl imidazole and Co(NO$_3$)$_2\cdot$6H$_2$O in an aqueous solution containing hexadecyltrimethylammonium bromide (CTAB).[142] A room-temperature one-pot stirring method was used for the preparation of graphene oxide (GO)-wrapped ZIF-67 nanocomposites with different concentrations of GO. The supercapacitance performance with respect to the specific capacitance and cyclic stability of the composite was better than those of pure GO or ZIF-67 nanocubes. 6 M KOH solution was utilized as the electrolyte to check the supercapacitance behaviour in a three-electrode system. In this ZIF-67 and ZIF-67/GO-*n* composite, direct involvement of two redox couples occurs, and a pseudocapacitor characteristic was observed. The faradaic reaction between Co^{2+}/Co^{3+} and Co^{3+}/Co^{4+} was implicated in the action. Upon an increase in scan rate, the specific capacitance value for all the composites decreases due to the limitation of ion diffusion rate. The composite containing 2 wt% of GO, *i.e.*, ZIF-67/GO-2, showed a specific capacitance of 100.47 F g^{-1} at a scan rate of 5 mV s^{-1}. The specific capacitance values of the ZIF-67/GO-*n* nanocomposites from the GCD data were higher than those of single GO or single ZIF-67. The specific capacitance value for the ZIF-67/GO-2 composite was 70.76 F g^{-1}
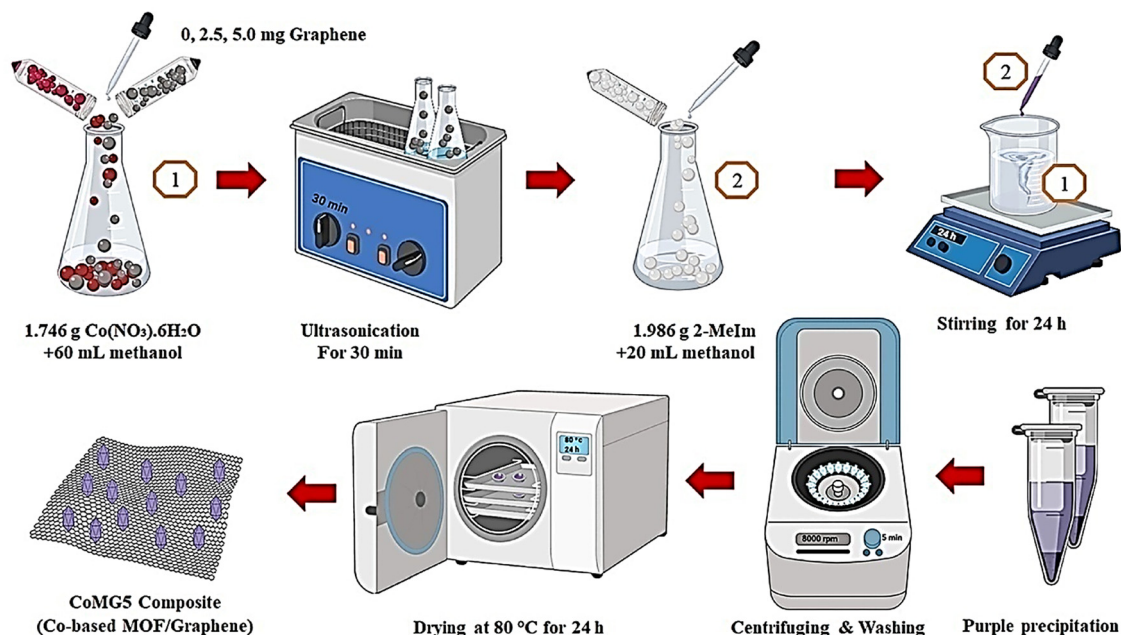
Fig. 5 The schematic production process of the CoMGX nanocomposites. Reproduced from ref. 143 with permission from Elsevier Ltd, Copyright 2021.

at a lower current density of 1 A g^{-1} and it reduced to 46.36 F g^{-1} at a current density of 20 A g^{-1}. A chronopotentiometry technique at 10 A g^{-1} was used to measure the cycle life of ZIF-67/GO-2. After performing the experiments for 600 cycles, ZIF-67/GO-2 exhibited an increase in capacitance value to 62.0 F g^{-1}, and thereafter, a minute rise in capacitance value was observed for cycles in the range 600 to 1000. The authors suggested that the activation of the ZIF-67/GO-2 composite over time is the reason behind the increase in capacitance value with the cycle charge–discharge process.

Azadfalah et al. demonstrated an in situ synthesis technique to prepare Co MOF/graphene composites using Co(NO$_3$)$_2$·6H$_2$O, methyl imidazole, and graphene (Fig. 5).[143]

Three-electrode systems were used to perform supercapacitor experiments in a 6 M KOH aqueous solution. Cyclic voltammetry experiments for all the samples were performed with a scan rate of 10 mV s^{-1} from −0.1 to 0.6 V (Fig. 6(a)). Here, capacitive performance is controlled by battery-like behaviour and redox reactions. The nitrogen adsorption–desorption analysis suggested that the effective surface area of the active materials is increased due to the addition of graphene to CoM. Also, the CV experiments revealed the reversibility and capacitive characteristics of all three substances at various scan rates from 10 to 100 mV s^{-1} (Fig. 6(b)–(d)). With the rise in scan rate, the lack of change in the CV curve indicated good capacitance behaviour due to the diffusion of ions in a faster mode onto the nanocomposites.

The discharge curve for all the electrodes in the GCD experiments showed nonlinear behaviour due to the redox reactions at the electrode–electrolyte interface, suggesting superior capacitance behaviour and a reversible nature in electrochemical performance. EIS measurements indicated that CoMG5 has the lowest charge transfer resistance, R_{ct}. All

the composites have lower R_{ct} values than CoM, which shows that the addition of graphene to CoM increases its electrical conductivity, and the reduction in resistance of the substance occurs through the facilitation of OH$^-$ ion diffusion into the active substance surface. The CoMG5 electrode showed the highest capacity of 549.96 F g^{-1} due to the synergic effect of Co MOF and graphene in the composite.

Srivastava and co-workers employed a cost-effective, simple mechanochemical synthesis method to synthesize a CoBTC/GNS composite with a high surface area using cobalt acetate, benzene-1,3,5-tricarboxylic acid (BTC), graphene oxide, and glucose.[144] The CoBTC/GNS composite showed low crystallinity owing to the presence of GNS. The generation of a sandwich structure confirms the presence of CoBTC MOF rods in between GNS. Due to this arrangement, the composite exhibited a specific capacitance of 608.2 F g^{-1} at a current density of 0.25 A g^{-1} in a 1 M KOH solution. At the time of potential scanning, the following quasi-reversible redox reactions occurred:

$$Co^{2+} + 3OH^- = CoOOH + H_2O + e^-$$

and

$$CoOOH + OH^- = CoO_2 + H_2O + e^-$$
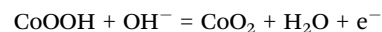
The combined effect of the pseudocapacitive and the double-layer behaviour of CoBTC and GNS delivers this high capacitance value, where 94.9% retention of capacitance was observed after the 2000th cycle. A high level of conductivity of the composite and consistent CoBTC MOF on GNS facilitate the quick movement of the electrolyte ions, which improves the electrochemical use of CoBTC, resulting in an outstanding capacitive performance of CoBTC/GNS. For practical application, a symmetric capacitor was assembled using CoBTC/GNS,
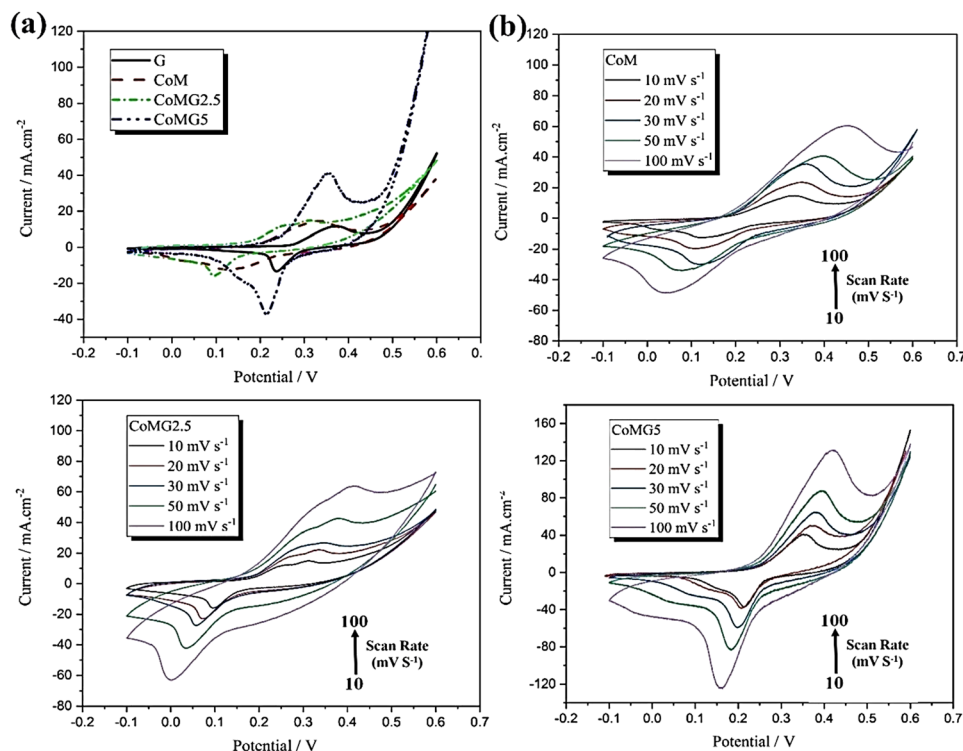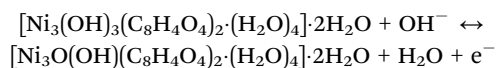
Fig. 6 The CV curves of (a) G, CoM, CoMG2.5, and CoMG5 at a scan rate of 10 mV s^{-1}, (b) CoM, (c) CoMG2.5 and (d) CoMG5 electrodes at different scan rates (10–100 mV s^{-1}) in 6 M KOH. Reproduced from ref. 143 with permission from Elsevier Ltd, Copyright 2021.

which showed a specific capacitance of 182.2 F g^{-1} with a power density and energy density of 1025.8 W kg^{-1} and 49.8 W h kg^{-1}, respectively. After performing 5000 charge–discharge cycles, there was 92.1% retention of original capacitance.

4.3.2 Ni-based MOF–graphene composite. Sedghi and co-workers synthesized a nanocomposite G@Ni-MOF using NiCl$_2$·6H$_2$O, H$_2$BDC, and graphene under solvothermal conditions.[145] From the CV curves, the obtained specific capacitance values were 148, 660, and 1017 F g^{-1} for G, Ni-MOF, and G@Ni-MOF, respectively, at a scan rate of 10 mV s^{-1} in 6 M KOH. The G@Ni-MOF electrode showed better storage capacity than Ni-MOF due to the battery-like character and faradaic redox reactions of the fabricated composite. The following equation is the reason for the pseudocapacitance response:

$$[Ni_3(OH)_3(C_8H_4O_4)_2\cdot(H_2O)_4]\cdot2H_2O + OH^- \leftrightarrow$$
$$[Ni_3O(OH)(C_8H_4O_4)_2\cdot(H_2O)_4]\cdot2H_2O + H_2O + e^-$$

The galvanostatic charge–discharge (GCD) curves were almost linear and triangular with a small angle, resulting from battery-type behaviour, exhibiting superior capacitive properties and electrochemical reversibility. Owing to the higher capacitance of these electrodes, the composite electrode displayed longer discharge times at the same current density. It has good cyclic stability, and 93.5% capacitance retention was observed after 1000 cycles. The increase in scan rates observed a little drop in the specific capacitance. This is due to the diffusion limiting current into the micropores. Asymmetric two-electrode systems were prepared using G@Ni-MOF and active carbon in 6 M KOH to utilize G@Ni-MOF in in-field applications. The as-prepared

two-electrode cell revealed a specific capacitance of 126.2 F g^{-1} and an energy density of 39.43 W h kg^{-1} at a power density of 34.29 W kg^{-1}, while this cell also displayed superb cycle life.

Using a facile hydrothermal method, Liu and co-workers synthesized Ni MOF nanospheres on reduced graphene oxide (Ni-MOF/rGO).[146] The material for supercapacitor application was prepared by annelation at 300 °C (Ni-MOF/rGO-300). Electrochemical performances of Ni-MOF/rGO-300, Ni-MOF/rGO, and Ni-MOF were studied with a scan rate of 100 mV s^{-1} in 6 M KOH. The confined spaces of Ni-MOF and Ni-MOF/rGO are smaller than that of Ni-MOF/rGO-300. In the presence of OH$^-$, all the electrodes exhibit oxidation and reduction peaks, with reversible redox reactions of Ni^{2+}/Ni^{3+}. In the GCD curves, Ni-MOF/rGO-300 displayed the greatest discharging process among the three modified electrodes. The obtained capacitance values at a current density of 1 A g^{-1} for Ni-MOF, Ni-MOF/rGO, and Ni-MOF/rGO-300 electrodes were 446, 529, and 954 F g^{-1}, respectively. The synergistic effects between Ni-MOF and rGO provide great capacity performance for the Ni-MOF/rGO-300 composite. The internal resistance R_S is smallest for the Ni-MOF/rGO-300 electrode, and its value is 0.56 Ω, resulting from the extremely aligned structure and additional reduction of GO by the calcination process. Ni-MOF/rGO-300 showed a specific capacitance of 954 F g^{-1} at 1 A g^{-1}. 80% retention of capacitance value was observed for the Ni-MOF/rGO-300 electrode after the 4000th charge–discharge cycle at 5 A g^{-1}. The potential application of Ni-MOF/rGO-300 was studied by fabricating an asymmetric supercapacitor using Ni-MOF/rGO-300.
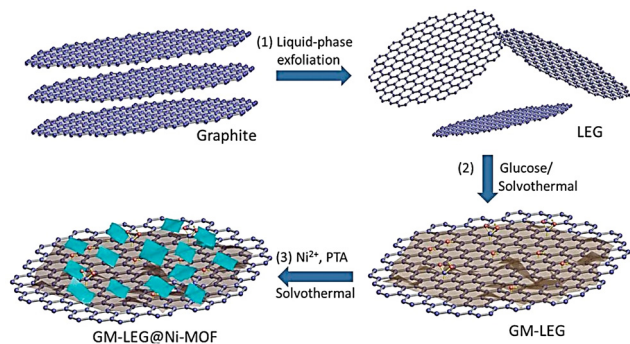
Scheme 1 Schematic synthesis procedure of GM-LEG@Ni-MOF composites. Reproduced from ref. 147 with permission from American Chemical Society, Copyright 2019.

Xiao et al. reported the development of a 2D LEG (graphene with low defect density and excellent electrical conductivity)-based Ni-MOF, GM-LEG@Ni-MOF, under solvothermal reaction conditions (Scheme 1).[147]

GM-LEG@Ni-MOF displayed a specific capacitance of 987.6 F g^{-1} when the current density was fixed at 0.5 A g^{-1} in 3 M KOH solution, where 85.6% retention of capacitance was observed after 3000 cycles. These results are better than those of the pure Ni-MOF and LEG@Ni-MOF counterparts. Abundant oxygen functionalities in LEG were achieved through the glucose modification protocol. Improvement in the solution processability of LEG and assistance to the controlled growth of Ni-MOF nanosheets around LEG are made possible by the presence of abundant oxygen functionalities. A higher amount of stable energetic sites was furnished due to the presence of a lamellar heterostructure. These energetic sites can boost the adsorption and transmission of ions and electrons in supercapacitor use.

Kim and co-workers synthesized Ni-MOF/rGO composite by using a hydrothermal method and used it in a supercapacitor application.[148] 6 M KOH was used to perform electrochemical supercapacitance experiments for rGO, Ni-MOF, and Ni-MOF/rGO. At a current density of 1 A g^{-1}, the observed specific capacitance values were 987.3 F g^{-1}, 8 F g^{-1}, and 847.3 F g^{-1} for MOF/rGO, rGO, and Ni-MOF, respectively. Ni-MOF/rGO exhibited a specific capacitance of 1154.4 F g^{-1} at a current density of 0.66 A g^{-1} with a discharge time of 885 s. After 3000 cycles, it showed 90% retention of the initial specific capacitance value. The increase in specific surface area and active sites of the electrode due to Ni MOF was the probable reason behind the higher value of the specific capacitance of the composite.

He et al. utilized Ni(NO$_3$)$_2$·6H$_2$O, graphene oxide (GO), and 4,4′-biphenyl dicarboxylic acid (BPDC) to synthesize Ni-BPDC/GO following a hydrothermal technique.[149] Detailed characterization of Ni-BPDC/GO was carried out using PXRD, SEM, Raman, and TEM analyses. The electrochemical performance of Ni-BPDC/GO and Ni-BPDC was studied in 6 M KOH solution in a three-electrode system. From the GCD curve, calculated specific capacitance values were 460 F g^{-1} and 630 F g^{-1} for Ni-BPDC and Ni-BPDC/GO-3, respectively, at 1 A g^{-1}. Ni(III) and

Ni(IV) redox couples are involved here. The EIS measurement values of charge transfer resistance (R_{ct}) were 5.96 Ω and 2.23 Ω for Ni-BPDC and Ni-BPDC/GO-3, respectively. To check the cyclic stability of the composite Ni-BPDC/GO-3, 10 000 cycles were performed at 5 A g^{-1}. For the first 2400 cycles, the capacitance value decreased due to Ni ions bonding with OH$^-$ ions. Then, the specific capacitance value remained constant, resulting in 56.5% retention of capacitance value after 10 000 cycles. An asymmetric supercapacitor was constructed for practical application purposes using rGO as the negative electrode and Ni-BPDC/GO-3 as the positive electrode in a two-electrode setup. The asymmetric supercapacitor exhibited the highest energy density of 16.5 W h kg^{-1} at a power density of 250 W kg^{-1}.

Das and co-workers recently synthesized Ni-MOF@GO composites with different wt% of GO.[150] The characterization of the composites was performed using PXRD, SEM, TGA, BET, and XPS analyses. Electrochemical experiments were performed using a three-electrode system in 6 M KOH. From the GCD experiment, the obtained specific capacitance value for IITKGP-20A-GO3 was ~840 F g^{-1} at 2 A g^{-1}. IITKGP-20A-GO3 revealed higher cyclic stability compared to the MOF when the stability was checked by performing 5000 GCD cycles at a current density of 15 A g^{-1}. The authors suggested that the increase in electrochemical redox active sites that are responsible for the fruitful transfer of the ions of the electrolytes and the inclusion of RGO lowered the resistivity of the composite through the synergistic effect of Ni-MOF and RGO sheets. For a real application, an asymmetric supercapacitor was fabricated. The two-electrode system showed a specific capacitance value of 111.4 F g^{-1} at 2 A g^{-1}. It supplied an energy density of 30.7 W h kg^{-1} at a power density of 388.5 W kg^{-1} with 84% capacitance retention after 7000 cycles. The constructed device can illuminate an LED light for about 3 minutes.

Chen et al. prepared GO/MOF composites (Ni-BTC@GO) through an in situ synthesis technique (Fig. 7) by varying the amount of GO sheets.[151]

They determined the amount of GO in Ni-BTC@GO by TG-DTG study. Electrochemical experiments were conducted in a three-electrode system utilizing 6 M KOH solution as an electrolyte (Fig. 8). For Ni-BTC@GO 2, the combined area of the CV curves is the highest (Fig. 8a). Fig. 8b illustrates GCD profiles at 1 A g^{-1}, with Ni-BTC@GO 2 having the most significant charge–discharge time. Fig. 8c displays Ni-BTC@GO 2 CV profiles with
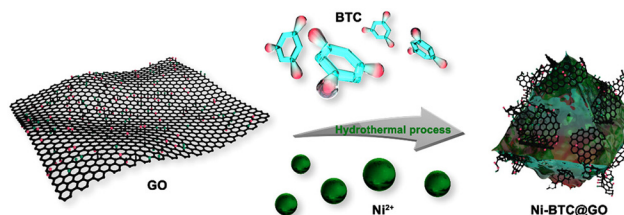

Fig. 7 The preparation process of Ni-BTC@GO composites. Reproduced from ref. 151 with permission from American Chemical Society, Copyright 2023.
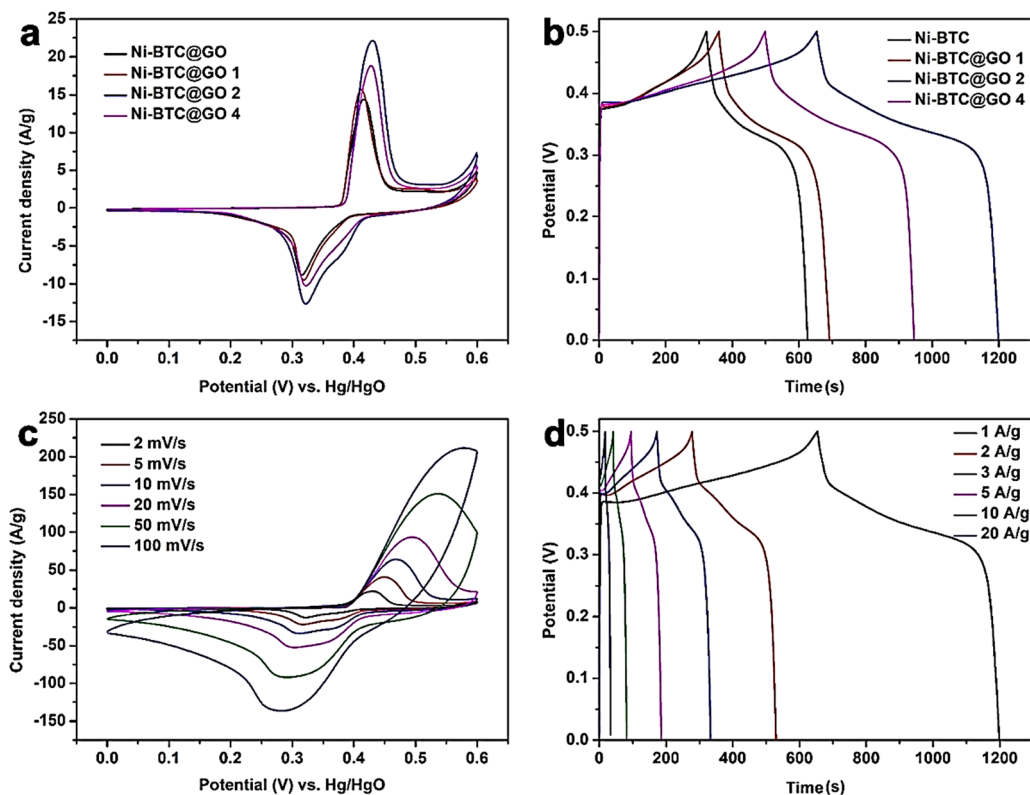
Fig. 8 (a) CV curves of Ni-BTC and Ni-BTC@GO composites at 2 mV s^{-1}, (b) GCD curves of Ni-BTC and Ni-BTC@GO composites at 1 A g^{-1}, (c) CV curves of Ni-BTC@GO 2 at 2–100 mV s^{-1}, and (d) GCD curves of Ni-BTC@GO 2 at 1–20 A g^{-1}. Reproduced from ref. 151 with permission from American Chemical Society, Copyright 2023.

scan rates varying between 2 and 100 mV s^{-1}. The change in the GCD profile with variation in current density for Ni-BTC@GO 2 is shown in Fig. 8d. The R_{ct} values were 7.649 Ω and 7.065 Ω for Ni-BTC and Ni-BTC@GO 2, respectively. Ni-BTC@GO 2 showed 84.47% retention of specific capacitance values after performing 5000 GCD cycles at 10 A g^{-1} current density. They also assembled an asymmetric capacitor, which exhibited an energy density of 40.89 W h kg^{-1} at 800 W kg^{-1}. They suggested that the conductivity of Ni-BTC is enhanced by the incorporation of GO sheets, resulting in a reduction in the ion transport path. This increases the specific capacitance values.

Khiew and coworkers reported new Ni-MOF/graphene nanocomposites for supercapacitor applications.[152] They synthesized MOFs with different morphologies in different solvents through a solvothermal method (Fig. 9). MOFs synthesized in a binary solvent mixture of ethylene glycol (EG) and DMF have a 3D flower-like morphology. Then, an Ni-MOF–graphene nanocomposite was prepared via the incorporation of graphene nanosheets into Ni-MOF. The as-synthesized Ni-MOF–graphene nanocomposite was characterized by PXRD, FESEM, EDX, TEM, FTIR, and TGA analyses. Electrochemical experiments were conducted in a two-electrode system using 2 M NaCl and 2 M KOH solutions as electrolytes. In 2 M NaCl electrolyte, the FG_Gr1.0, nanocomposite exhibited a specific capacitance of 111.68 F g^{-1} at 0.3 A g^{-1}. In 2 M KOH, the specific capacitance for the FG_Gr1.0 nanocomposite was 126.21 F g^{-1} at a current

density of 0.3 A g^{-1}. 14.68 W h kg^{-1} and 291.82 W kg^{-1} were the energy density and power density for FG_Gr1.0 in 2 M NaCl, respectively. 97.70% retention of capacitance and Coulombic efficiency of 89.05% were obtained after carrying out 10 000 GCD cycles at a current density of 1.5 A g^{-1} in 2 M NaCl compared to electrode materials synthesized in other solvent systems. The 3D flower-like morphology of the MOF assists the process of ion transfer and produces a large disclosed surface to store a huge number of charges. At the same time, a reduction in intrinsic electrochemical resistance is possible due to the benefit of the unique structure resulting in an enhancement in supercapacitance performance. Besides that, the incorporation of highly conductive graphene nanosheets further increases the supercapacitor behaviour.

4.3.3 Cu-based MOF–graphene composites. A Cu-MOF/G composite was synthesized by Azadfalah *et al.* using graphene, Cu(NO$_3$)$_2$·3H$_2$O, and 1,3,5-benzene tricarboxylic acid under facile solvothermal conditions.[153] The characterization of the Cu-MOF/G composite was carried out via PXRD, FESEM, TEM, BET, Raman, and FTIR analyses. Cyclic voltammetry experiments were performed for G, Cu-MOF, and Cu-MOF/G to compare the results of using a 6 M KOH solution in water as an electrolyte. The specific capacitance values were 148, 190, and 482 F g^{-1} for graphene, Cu-MOF, and Cu-MOF/G at a scan rate of 10 mV s^{-1}. The better performance of Cu-MOF/G compared to Cu-MOF is due to the faradaic and battery-type
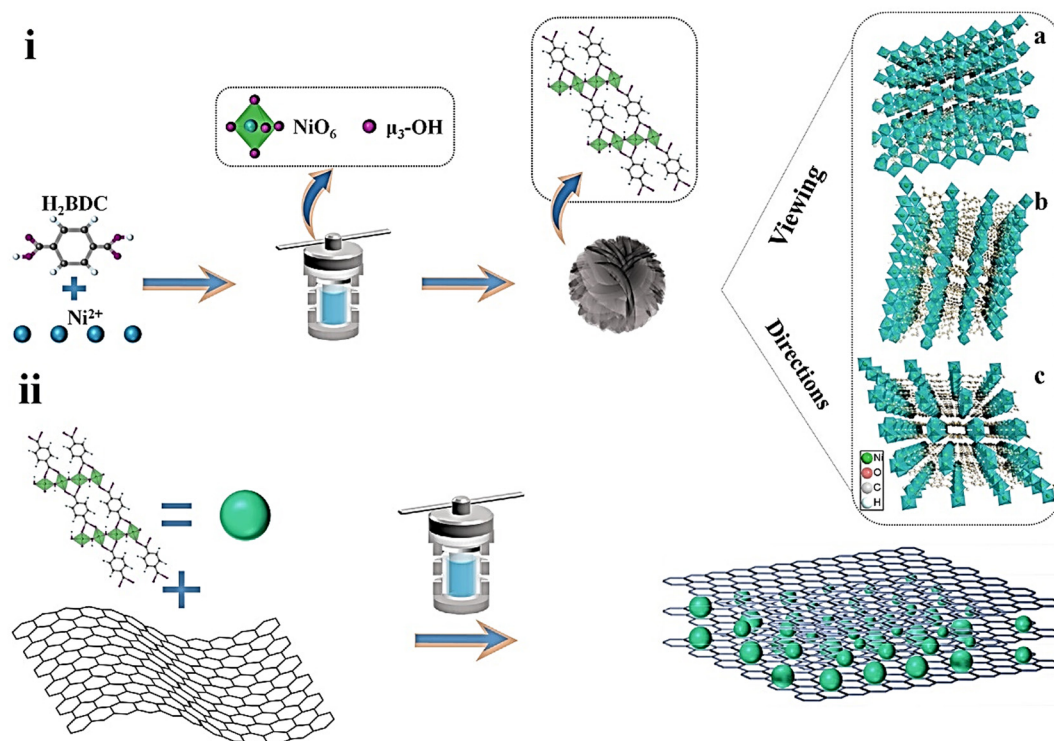
Fig. 9 Schematic illustration of the fabrication of (i) hierarchical Ni–MOFs and (ii) FG_Gry *via* a solvothermal method. Reproduced from ref. 152 with permission from Elsevier Ltd, Copyright 2022.

characteristics. The composite showed good cyclic life, with 93.8% capacitance retention after 1000 cycles at a current density of 0.3 A g^{-1}. The CV curve showed a hysteresis shape with redox peaks. The synergistic effects of Cu-MOF and graphene provide better retention ability and specific capacitance to Cu-MOF/G. The GCD data suggested a specific capacitance of 430 F g^{-1} at a current density of 1 A g^{-1} for Cu-MOF/G. The nonlinear charge–discharge curve confirms the battery-like behaviour of the sample. Cu-MOF/G and activated carbon were utilized as the positive and negative electrodes for assembling an asymmetric supercapacitor in 6 M KOH electrolyte. The asymmetric supercapacitor furnished a high energy density of 34.5 W h kg^{-1} and a power density of 1350 W kg^{-1} at a current density of 0.5 A g^{-1}.

Rai and co-workers synthesized a Cu-MOF (HMRL-1) using a tetracarboxylic-acid-based ligand H$_4$L (3,3′,5,5′-tetracarboxy-diphenylmethane) (5,5′-MDIP ligand) as linker with Cu(NO$_3$)$_2$·3H$_2$O under solvothermal conditions.[154] The fabrication of the composite (HMRL-1/R) was done using the as-synthesized MOF and reduced graphene oxide (R) through a simple ultra-sonication approach (see Scheme 2). The 3D porous MOF with a suitable channel structure and redox-active Cu^{2+} centres enhanced the ion transport. The electrochemical performance of the composite showed hybrid capacitive features due to the combination of the EDLC behaviour of rGO and pseudocapacitive behaviour of Cu-MOF, respectively, where 366.6 F g^{-1} specific capacitance was observed at a current density of 1 A g^{-1} in 1 M Na$_2$SO$_4$. After performing 4000 cycles, 83.30% retention
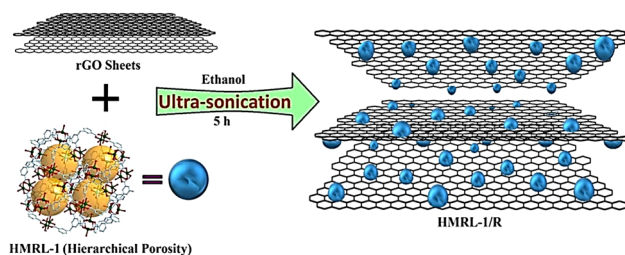
Scheme 2 Synthesis of HMRL-1/R. Reproduced from ref. 154 with permission from Elsevier Ltd, Copyright 2021.

of capacitance was observed. These results are far better than those of HMRL-1 or R. In addition, preventing restacking of 2D rGO sheets increases the production area for ion adsorption due to the presence of MOFs in the rGO matrix.

The acoustomicrofluidic method was used by Ehrnst *et al.* to synthesize homogeneous quasi-2D MOF–graphene oxide (q-2D-MOF/rGO) planar heterostructures without requiring conductive binders or scaffolds.[155] The quasi-2D MOFs have a high surface area to volume ratio and dense exposure of Cu sites on their surface, which increases effective Cu/GO coordination and reduces GO to reduced graphene oxide (rGO) without disturbing the structural characteristics of the MOF. A detailed characterization of the composite was performed using PXRD, FTIR, TGA, XPS, Raman spectroscopy, helium ion microscopy, and BET analyses. A three-electrode arrangement in 1 M H$_2$SO$_4$

electrolyte solution was used to perform the supercapacitor experiments. The composite exhibited a quasi-rectangular shape in cyclic voltammetry due to the attribution of the rGO and Cu-BTC MOF components. A deviation in GCD data from the triangular trace of double-layer capacitance was observed. The composite exhibited a gravimetric capacitance of 292 F g^{-1} at a current density of 1 A g^{-1}.

Mohanadas et al. reported the preparation of a Cu-MOF and rGO composite, namely MrGO, for supercapacitor applications.[156] MrGO was characterized by PXRD, FESEM, FTIR, and Raman spectroscopy. A three-electrode setup was utilized to perform supercapacitor experiments in 1 M KCl. The MrGO electrode exhibited a specific capacitance of 208.9 F g^{-1}, which was quite large in comparison to those of Cu-MOF of 143.7 F g^{-1} or rGO of 100.2 F g^{-1}. The charge transfer resistance (R_{ct}) value of 0.95 Ω was much lower than those of Cu-MOF or rGO. An asymmetric device was prepared using vanadium oxide/reduced graphene oxide (VrGO) as the positive electrode and MrGO composite as the negative electrode. This device worked over a wide potential range (0–1.4 V) and exhibited a specific capacitance of 483.9 F g^{-1} at a scan rate of 5 mV s^{-1}. It exhibited good specific energy and specific power of 31.2 W h kg^{-1} and 656.4 W kg^{-1}, respectively. The asymmetric device retained 92% of its initial capacitance after performing 4000 CV cycles.

Krishnan et al. used porous piperazine (N) functionalized Cu-MOF (C) and reduced graphene oxide (R) for the fabrication of a hybrid composite Cu-MOF/rGO (CR) using simple

ultrasonication.[157] Cu-MOF/rGO was characterized by PXRD, FTIR, TGA, SEM, TEM, and BET analyses. CV and GCD experiments were carried out for Cu-MOF, reduced graphene oxide, and hybrid composite Cu-MOF/rGO (CR) using a three-electrode arrangement in 1 M Na$_2$SO$_4$ solution. A detailed description of the GCD experiments is given in Fig. 10. Fig. 10(a) compares the GCD profiles for C-GCE, R-GCE, and CR-GCE at 1 A g^{-1}. From the charge–discharge data, the obtained values of specific capacitances were 867.09, 284.41, and 135 F g^{-1} for CR-GCE, R-GCE, and C-GCE at a current density of 1 A g^{-1} (Fig. 10(b)). Fig. 10(c) shows the GCD curves for CR-GCE at various current densities. The fluctuation in the specific capacitances for C-GCE, R-GCE, and CR-GCE depending on the current density is shown in Fig. 10(d).

The high specific capacitance of CR-GCE is due to the fact that the synergistic effect of R and C allows lower internal resistance, increases ion diffusion, enhances charge transfer kinetics, and provides a larger active surface area. CR showed 131.65% retention of the initial specific capacitance after performing the GCD experiments for 5000 cycles. They showed that at the time of the cycling process, electrochemical activation of the CR composite occurs, increasing the surface wettability and active electrochemical sites, resulting in a higher specific capacitance. As a result, the electrolyte–electrode interaction increases and enhances the efficient diffusion of electrolyte ions into the electrodes. For a real application, a symmetric supercapacitor device was assembled using the CR composite. This device exhibited a maximum energy density of
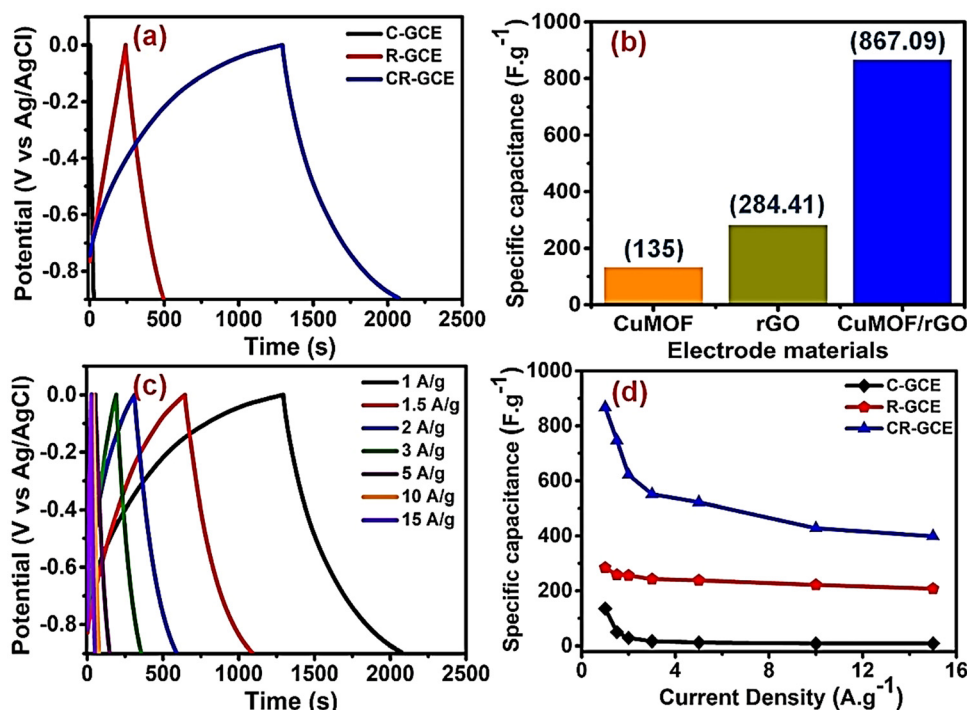

Fig. 10 (a) Comparison of the GCD profiles of C-GCE, R-GCE, and CR-GCE at 1 A g^{-1} current density in 1 M Na$_2$SO$_4$; (b) specific capacitances of C-GCE, R-GCE, and CR-GCE electrodes at 1 A g^{-1}; (c) GCD profiles of CR-GCE at different current densities (1–15 A g^{-1}); and (d) specific capacitance variations of C-GCE, R-GCE, and CR-GCE with changing current densities (1–15 A g^{-1}). Reproduced from ref. 157 with permission from Elsevier Ltd, Copyright 2022.

30.56 W h kg^{-1} at a power density of 0.6 kW kg^{-1}. A maximum power density of 12 kW kg^{-1} was observed at an energy density of 14.59 W h kg^{-1}. The symmetric device showed 90.07% conservation of capacitance after carrying out 10 000 charge–discharge cycles.

Sawangphruk and co-workers reported the synthesis of a reduced graphene oxide–MOF composite (10 wt% rGO/HKUST-1) through the utilization of 10 wt% rGO and HKUST-1.[158] The BET surface area, specific pore volume, and average pore diameter of 10 wt% rGO/HKUST-1 were 1241 m^2 g^{-1}, 0.78 cm^3 g^{-1}, and 8.2 nm. This pore size is suitable for uptaking and releasing electrolytes. Here, 0.5 M Na$_2$SO$_4$ solution was used as an electrolyte. 10 wt% rGO/HKUST-1 coated on flexible carbon fiber paper (CFP) was used as an electrode in a three-electrode configuration. The 10 wt% rGO-HKUST-1 composite showed a specific capacitance of 385 F g^{-1} at a current density of 1 A g^{-1}. This mesoporous 10 wt% rGO-HKUST-1 composite has sufficient well-ordered tunnels suitable for the insertion/extraction of hydrated Na$^+$ and H$_3$O$^+$ into/from the electrode. A symmetrical supercapacitor set-up of 10 wt% rGO/HKUST-1 showed a specific energy of 42 W h kg^{-1} and a specific power of 3100 W kg^{-1}. 98.5% retention of capacitance occurred after 4000 cycles.

4.3.4 Fe-based MOF–graphene composites. Hu and co-workers reported the preparation of a growth-oriented Fe-based MOF synergized with a GA composite for performing supercapacitor applications.[159] A solvothermal method was used to grow MIL-88-Fe on the surface of graphene in its (002) plane. An oriented MOF/GA composite has advantages like fast charge–discharge rates, high capacitive volumes, and cycling stability. In one preparation of MIL-88 in the as-synthesized graphene aerogel (GA), spindle-like MOF was produced, which was labeled GAMOF. Another sample was prepared using GAMOF(Fe^{3+}) with an oriented rod-like MOF. In an aqueous graphene oxide (GO) solution, introducing Fe^{3+} ions produces Fe^{3+}-doped GAs. The manageable and directional growth of the MOF is possible due to the coupling of a π electron in graphene with the electrophilic Fe^{3+} ion (ionic radius 0.064 nm) *via* p–π interaction. As can be seen from the SEM and TEM analyses of GA, GAMOF, and GAMOF(Fe^{3+}) composites, the MOF morphology and distribution in the composite were examined (see Fig. 11). The SEM images show that GA, GAMOF, and GAMOF(Fe^{3+}) have dissimilar morphological patterns (see Fig. 11(a)–(c)). HRTEM images of GAMOF(Fe^{3+}) suggest that it has a highly crystalline structure (Fig. 11(d)). The growth of the MOF in the [022] direction is confirmed by analyzing the interplanar distance, which shows that the (002) face is assembled along the MIL-88-Fe growth axis.

The as-prepared materials were characterized through XRD, IR, and XPS. Cyclic voltammetry experiments were performed for GA, GAMOF, and GAMOF(Fe^{3+}). The increased capacitance changes of GAMOF and GAMOF(Fe^{3+}) are mainly due to the alteration of electric double-layer properties as affected by MOF. For GA and GAMOF(Fe^{3+}), the charge–discharge profile is symmetric, whi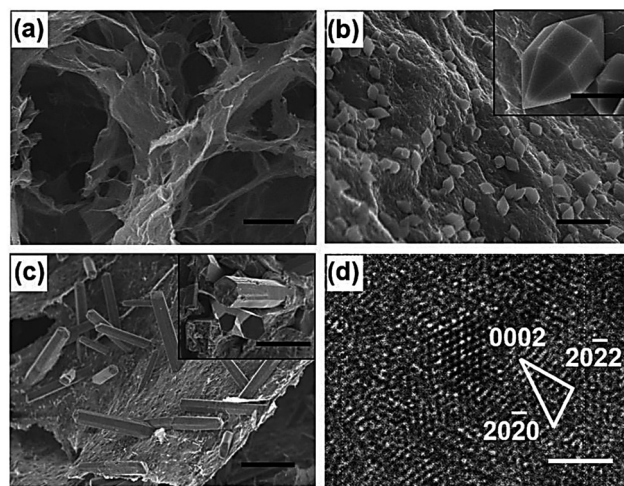le for GAMOF, the charge–discharge profile is asymmetric. The asymmetric nature comes out due to some irreversible faradaic processes. The transport of ions and channels for diffusion was found in the mesopores and micro-pores of GA, and the storage of ions was obtained from the micropores of MOF, where the retention ratios for GA, GAMOF, and GAMOF(Fe^{3+}) were 66.2, 44.7 and 74.4%, respectively, after 10 000 cycles.

4.3.5 Zn-based MOF–graphene composites. Zn-MOF and reduced graphene oxide (rGO) hybrid composites (Zn-MOF–rGOs) with wrinkled nanosheet-like structures were synthesized by Sohn and coworkers using a hydrothermal process[160] Nanocomposites of rGO and Zn-MOF were synthesized at weight percentage ratios (rGO:precursor Zn(NO$_3$)$_2$·6H$_2$O) of 10 : 100 and 20 : 100, and indexed as Zn-MOF–rGO$_{10}$ and Zn-MOF–rGO$_{20}$, respectively. The electrochemical behaviour of the composites was studied in a 3 M KOH solution using a three-electrode configuration. The Zn-MOF–rGO$_{20}$ electrode showed a specific capacity of 205 C g^{-1} at a current density of 1 A g^{-1}. A symmetric device with a Zn-MOF–rGO$_{20}$ electrode showed a specific energy density of 7.1 W h kg^{-1} at a power density of 0.4 kW kg^{-1}. A charge transfer resistance (R_{ct}) value of 5.95 Ω was observed at the electrode–electrolyte interface of the Zn-MOF–rGO$_{20}$ symmetric device. Using power law, they observed that the diffusion-controlled pathway of the electrochemical charge storage mechanism contributes more than the pseudocapacitive-controlled pathway. The authors suggested that the synergistic effect between ZnMOF and rGO is the reason behind the supercapacitance performance. Firstly, a commendable pathway for the transfer of charge and an active surface area were obtained due to the porous Ceratophyllum-like surface structure of ZnMOF. Secondly, electron transfer during the charge–discharge process is promoted by attaching

Fig. 11 SEM and TEM images of GA, GAMOF, and GAMOF(Fe^{3+}) composites. (a) SEM image of GA (scale bar: 20 μm). (b) Low- (scale bar: 2 μm) and high-magnification SEM images (inset; scale bar: 500 nm) of GAMOF. (c) Low- (scale bar: 2 μm) and high-magnification SEM images (inset, scale bar: 500 nm) of GAMOF(Fe^{3+}). (d) HRTEM image of GAMOF(Fe^{3+}) (scale bar: 2 nm). Reproduced from ref. 159 with permission from WILEY-VCH, Copyright 2018.

electrically conductive components to the rGO sheets, resulting in good supercapacitor behaviour. In addition, the porous rGO increases the surface area for electrolyte–electrode contact, boosting the supercapacitor performance of the composite.

4.3.6 Zn-based and Co-based MOF–graphene composites. Using an ultrasonic method, Zhang et al. prepared other graphene oxide composites: ZIF-8/GO and ZIF-67/GO.[161] Systematic characterization was performed using PXRD and SEM. TEM and BET analyses. The electrochemical behaviour of both samples was studied in a 6 M KOH solution. Cyclic Voltammetry studies of ZIF-8, ZIF-8/GO, ZIF-67, ZIF-67/GO and GO were carried out at different scan rates (see Fig. 12).

The pseudocapacitance properties of ZIF and ZIF/GO composites were confirmed from their CV curves. The shift of cathode peaks to higher voltage and the shift of anodic peaks to lower values occurred when the scan rate increased. At a higher scan rate, an increase in electric polarization and an irreversible reaction are the reasons behind the cathodic and anodic peak shifts. The specific capacitance of ZIF-8/GO was 160 F g⁻¹ with a scan rate of 5 mV s⁻¹. The authors observed that the specific capacitance value of the ZIF-8/GO composite increased with a rise in scan rate, which was more than twice that of ZIF-8. So, the specific capacitance of the ZIF-67/GO electrode material was 252 F g⁻¹, greater than that of ZIF-67 of 189 F g⁻¹. The GCD curves are nonlinear for all the samples, indicating that the samples behave like pseudocapacitors. ZIF-67/GO showed much higher (202 F g⁻¹) capacitance at a current density of 1 A g⁻¹ than ZIF-8/GO (95 F g⁻¹) or GO (73 F g⁻¹). However, two reasons are responsible for the excellent supercapacitor performance: the good conductive feature of GO

assists ion diffusion and electron transport into the redox area of the composite.

Additionally, the very good porous structure and large surface area of ZIF-67 furnish high energy storage capacity. In pure ZIF, the distribution is less than that of ZIF developed on GO, and the active centres in ZIF are less than those of ZIF/GO, which enhances the capacitance of the electrode material. The ZIF-8/GO composite has a lower R_S value (0.5 Ω) than ZIF-8 (0.7 Ω). The cyclic stability of the ZIF-8/GO and ZIF-67/GO electrodes was measured at a scan rate of 10 mV s⁻¹. The excellent cyclability and good rate capability of the ZIF-67/GO composite for pseudocapacitors were confirmed by the slight increase in capacitance value during 600 cycles.

4.3.7 Zr-based MOF–graphene composites. Jayaramulu et al. reported the covalent attachment of an amine-functionalized MOF (UiO-66-NH₂) to the basal plane of carboxylate-functionalized graphene acid (GA) by forming an amide bond (Fig. 13(a) and (b)).[162] The composite GA@UiO-66-NH₂ possesses a high surface area, an interconnected conductive network, and hierarchical pores. Octahedral GA@UiO-66-NH₂ nanocrystals provide the micropores. The GA–GA interlayer distance, which is grown via a covalent bond of GA with the MOF spacers through an amide, provides mesoporosity in the composite. The composite retains all the characteristic peaks of pristine UiO-66-NH₂, proving that the crystal structure remained undisturbed after anchoring to GA (see Fig. 13(c)). The formation of amide between the amino groups of MOF and carboxylate groups of GA was confirmed by XPS spectroscopy. A BET experiment revealed that the specific surface area was 600 m² g⁻¹ with a large pore volume of 1.09 cm³ g⁻¹ (see Fig. 13(d)).
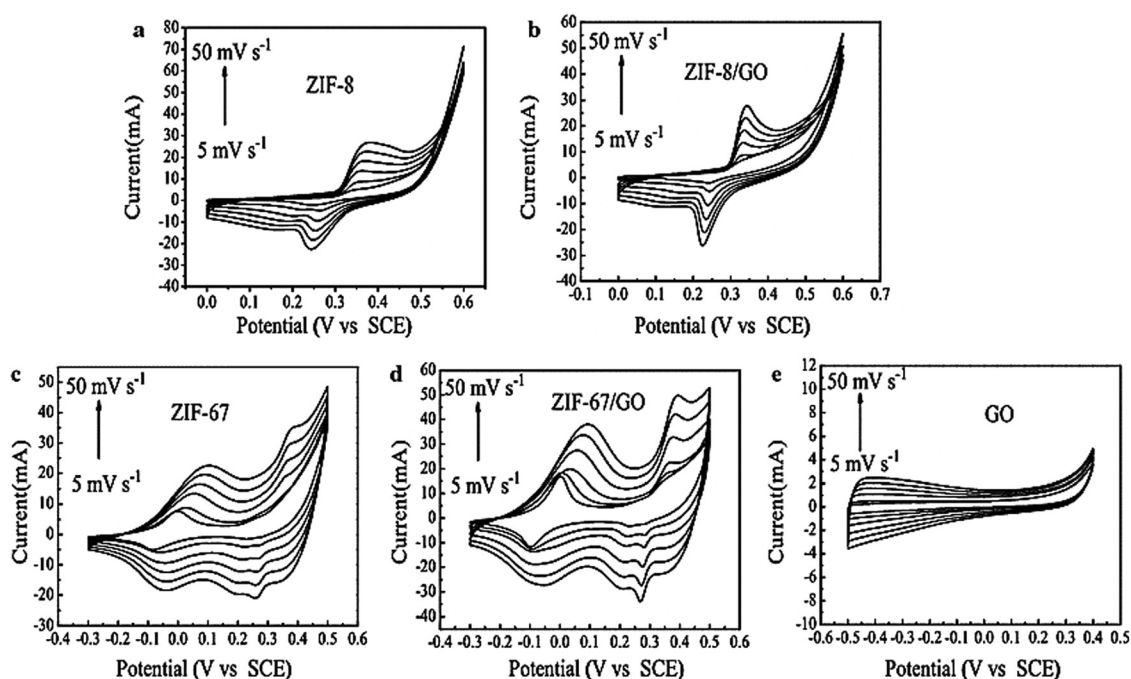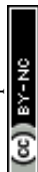

Fig. 12 Cyclic voltammetry curves of (a) ZIF-8, (b) ZIF-8/GO, (c) ZIF-67, (d) ZIF-67/GO, and (e) GO at increasing voltage scan rates of 5, 10, 20, 30, 40, and 50 mV s⁻¹. Reproduced from ref. 161 with permission from Springer Science, Copyright 2016.
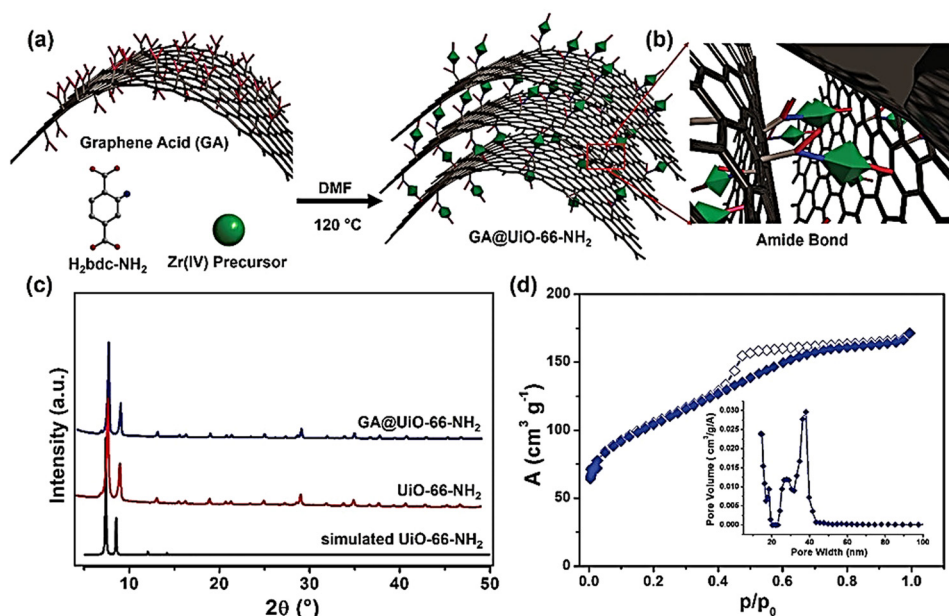
Fig. 13 (a) Schematic illustration of the covalent assembly of GA and UiO-66-NH$_2$ into GA@UiO-66-NH$_2$ under solvothermal conditions *via* (b) amide bonds. Carbon, oxygen, and nitrogen are represented in grey, red, and blue, respectively. Hydrogens have been omitted for clarity. Green octahedra represent UiO-66-NH$_2$ nanocrystals. (c) PXRD patterns of UiO-66-NH$_2$ (black simulated pattern, red measured pattern) and GA@UiO-66-NH$_2$ (blue pattern). (d) N$_2$ adsorption isotherm of GA@UiO-66-NH$_2$ measured at 77 K; filled symbols represent adsorption, empty symbols desorption. The inset shows the pore size distribution determined through the NLDFT method. Reproduced from ref. 162 with permission from WILEY-VCH, Copyright 2021.

However, the HAADF TEM image of composite GA@UiO-66-NH$_2$ exhibited a regular distribution of Zr, N, C, and O all over the sample. A three-electrode system was utilized to perform electrochemical experiments in 1 M Na$_2$SO$_4$. The shape of the CV curve is not fully rectangular, which suggests a charge contribution from the pseudocapacitive mechanism. This pseudocapacitive property may originate due to the stabilization of nitrogen-based functional amide groups on GA@UiO-66-NH$_2$. At a current density of 2 A g^{-1}, the obtained specific capacitance was 651 F g^{-1}. Charge–discharge data collection at a very high current density demonstrated high rate performance. An asymmetric device was set up using Ti$_3$C$_2$T$_x$ Mxene as a negative electrode and GA@UiO-66-NH$_2$ as a positive electrode. This device showed high-energy battery-like and high-power capacitive properties with a power density of up to 16 kW kg^{-1} and an energy density of up to 73 W h kg^{-1}. The devices exhibited 88% retention of their initial capacitance over 10 000 cycles.

4.3.8 Al-based MOF–graphene composites. Majumder *et al.* prepared an aluminum-based MOF, MIL-53(Al), and reduced graphene oxide (rGO) composite, abbreviated as MIL-53(Al)@rGO, for supercapacitor application.[163] A two-step solvothermal technique was used to synthesize MIL-53(Al)@rGO. 1 M KOH solution was used as an electrolyte for the measurement of electrochemical experiments of C-1 (MIL-53 (Al)), C-100 (rGO), and MIL-53(Al)@rGO hybrid composites (C-2 to C-50) in a three-electrode system. CV and GCD measurements were carried out. The maximum specific capacitance of 280 F g^{-1} was acquired for the C-10 composite from GCD measurements at 0.5 A g^{-1}. The C-10 composite

showed the highest specific capacitance due to the synergistic effect, which allows the exposure of more active sites, enhancing charge transport, and higher contact of electrolyte with the electrode. To test for practical application of the MIL-53(Al)@rGO composite, a symmetric two-electrode system was constructed. The specific capacitance for the C-10 composite was 75 F g^{-1}. C-10 exhibited an energy density of 6.66 W h kg^{-1} at a power density of 200 W kg^{-1} with a current density of 0.5 A g^{-1}. 50% cyclic stability was obtained for the C-10 composite after performing 5000 GCD cycles at a current density of 3 A g^{-1}.

4.3.9 N-doped Co-based MOF–graphene composites. Park and co-workers studied the supercapacitance performance of N-doped ZIF-67 and reduced graphene oxide composite (N-ZIF-67·rGO) prepared through an *in situ* technique.[164] Three-electrode arrangements were utilized to conduct supercapacitor-based experiments in a 2 M KOH solution. The electrochemical responses of bare Ni foam (NF), N-ZIF-67/NF, and N-ZIF-67·rGO/NF are provided in Fig. 14. Fig. 14(A) shows the CV responses of N-ZIF-67/NF, N-ZIF-67·rGO/NF, and bare Ni foam (NF). The CV behaviour of N-ZIF-67·rGO/NF is depicted in Fig. 14(B). It came to light that the peak electrical current increased considerably when the scan rate was raised, indicating that there was an appropriate linear correlation between the anodic and the cathodic peak electrical currents with scan rate (Fig. 14(C)). The GCD profiles of N-ZIF-67/NF and N-ZIF-67·rGO/NF at a fixed current density of 20 mA are shown in Fig. 14(D).

Here, the redox peaks and pseudocapacitive features of Co MOFs were associated with the reversible transition of Co^{3+} and
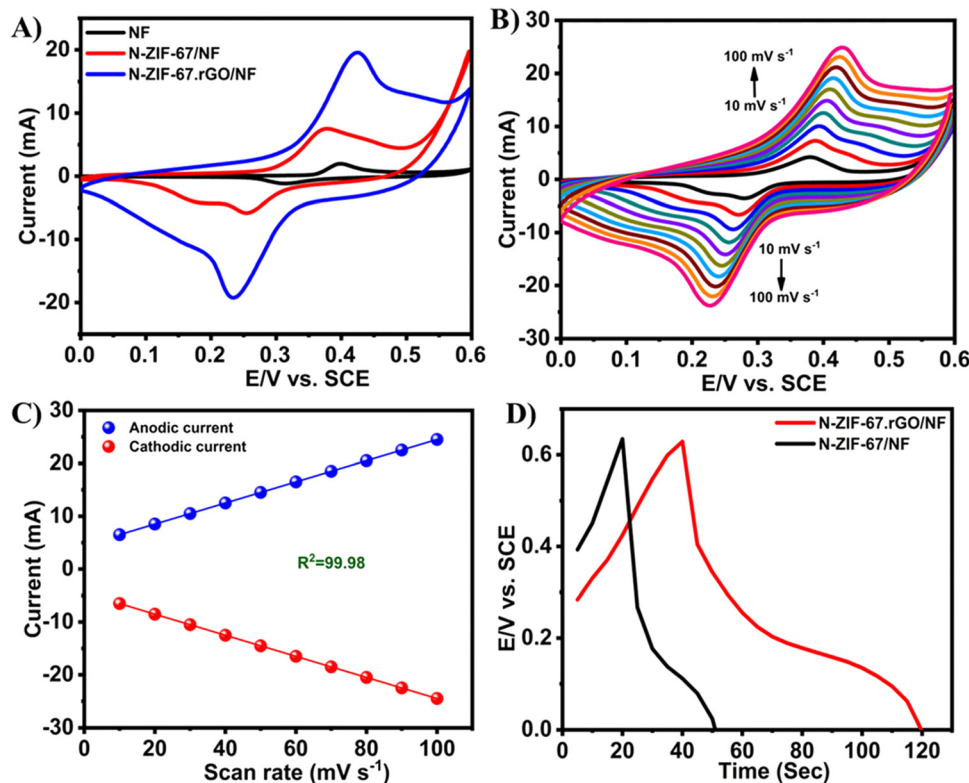
Fig. 14 CV curves of bare NF, N–ZIF-67/NF, and N–ZIF-67·rGO/NF in 2 M KOH with a scan rate of 50 mV s^{-1} (A), CV curves of NZIF-67·rGO/NF in 2 M KOH at different scan rates (B), anodic and cathodic peak currents for N–ZIF-67·rGO/NF as a function of scan rate (C), and GCD curves of N–ZIF-67/NF and N–ZIF-67·rGO/NF in 2 M KOH at a current density of 20 mA (D). Reproduced from ref. 164 with permission from American Chemical Society, Copyright 2021.

Co^{2+}. The following equations show the probable mechanism for the pseudocapacitance response:

$$Co_3O_4 + OH^- + H_2O \leftrightarrow 3CoOOH + e^-$$

and

$$CoOOH + OH^- \leftrightarrow CoO_2 + H_2O + e^-$$
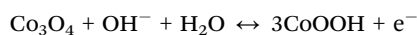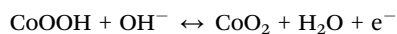
GCD experiments suggested that the specific capacitance values were 212 and 962 F g^{-1} for N–ZIF-67/NF and N–ZIF-67·rGO/NF, respectively, at 20 mA cm^{-2}. Synergistic effects between the rGO and N–ZIF-67 MOF active sites were responsible for the superior supercapacitance performance of N–ZIF-67·rGO/NF. 97% retention of specific capacitance occurred after performing the GCD experiments for 1000 cycles. A two-electrode set-up was also prepared for practical application purposes, and battery-type supercapacitor characteristics were observed.

4.3.10 Ni-doped Zn-based MOF–graphene composites. Majumder and co-workers performed the synthesis of 50% Ni-doped MOF-5 based composite with reduced graphene oxide (rGO) by dispersing rGO in a mixture of dimethyl-formamide (DMF) and chlorobenzene solution with varying weight percentages of rGO (5, 10, 30, and 50%) (Scheme 3).[165] Characterization was performed using PXRD, SEM, TEM, EDX, and BET analyses. The surface area of MOF decreases upon rGO

addition, and the formation of new pores at the MOF/rGO increases the pore volume of the MOF.

MOF-5$_{Ni50\%}$ and MOF-5$_{Ni50\%rGO50\%}$ were used for electro-chemical performance. MOF-5$_{Ni50\%}$ showed well-separated redox peaks, but for MOF-5$_{Ni50\%rGO50\%}$, an anodic peak and a broad cathodic response were observed. The double-layer charging behaviour from the rGO nanosheets covers the faradaic region, resulting in a broad cathodic response. The capacitance value of MOF-5$_{Ni50\%rGO50\%}$ was found to be 758 F g^{-1} due to the synergistic interaction between rGO and MOF. The redox peak separation is about 122 mV, suggesting that the mechanism is the two-electron pathway. An efficient charge transfer occurred due to the combined effort of inter-connected graphene nanosheets and distributed Ni centres in MOF-5.

4.3.11 Mg-doped Cr-based MOF–graphene composites. Farisabadi *et al.* synthesized Mg-doped Cr-based MOF (MIL-101(Cr)) and a reduced graphene oxide composite MIL-101(Cr,Mg)/rGO to study its electrochemical supercapacitor performance.[166] A three-electrode configuration in 6 M KOH solution was employed to perform the supercapacitor experiments. Cyclic voltammetry experiments indicated that the MIL-101(Cr,Mg)/rGO electrode has an extra cathodic peak in comparison to MIL-101(Cr)/rGO. The following equations were responsible for the electrochemical activity of MIL-101(Cr,Mg)/rGO:
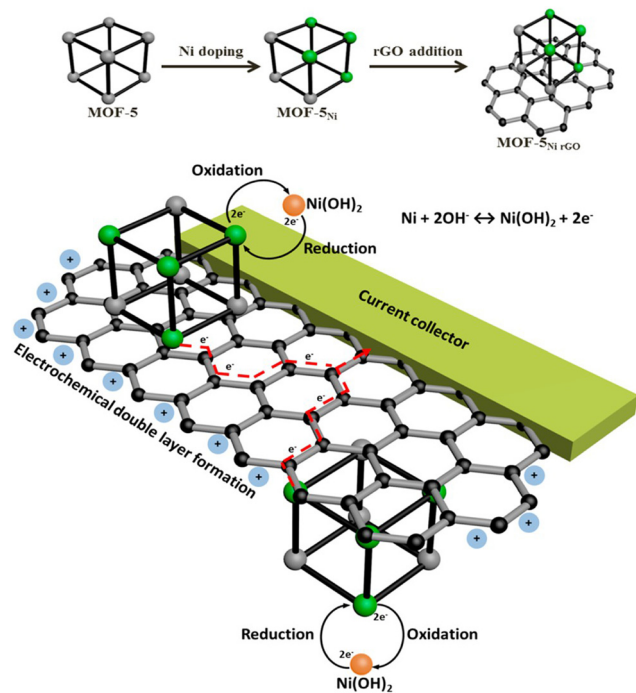
Scheme 3 The concept for Ni doping and incorporating rGO to form a composite of rGO and Ni-doped MOF-5 and its use as an electrode material that harnesses both the electrochemical double layer performance of rGO and the reversible redox reactions of Ni metal centres with a synergy that facilitates effective and efficient charge transfer processes. Reproduced from ref. 165 with permission from American Chemical Society, Copyright 2015.

$$Cr(III) + OH^- = Cr(II)$$

$$Mg^{2+} + 2OH^- = Mg$$

and

$$Cr^{2+} + 2OH^- = Cr$$

From the GCD curve, the calculated values of specific capacitance for MIL-101(Cr,Mg)/rGO and MIL-101(Cr)/rGO electrodes at a current density of 1 A g^{-1} were 261.41 F g^{-1} and 137.46 F g^{-1}, respectively. An asymmetric supercapacitor device was fabricated for in-field application purposes using activated carbon as the negative electrode and MIL-101(Cr,Mg)/rGO as the positive electrode. An energy density of 4.65 W h kg^{-1} and power density of 7653 W kg^{-1} were obtained from this device. After 2000 cycles, 86% retention of capacitance occurred.

4.3.12 Ni–Co MOF–graphene composites. Beka *et al.* prepared NiCo-MOF-based 2D nanosheet (NiCo-MOF)/reduced graphene oxide by a one-step room-temperature precipitation method using Co(NO$_3$)$_2$·6H$_2$O, Ni(NO$_3$)$_2$·6H$_2$O, 2-methyl imidazole, and reduced graphene oxide (rGO).[167] Here, NiCo-MOF with highly disclosed active sites can behave like a pseudocapacitive material, while rGO can act as the ionic and conductive pathway. Four different samples were prepared depending on the concentration of rGO, keeping the concentration of MOF constant, namely NiCo-MOF/rGO-O,

NiCo-MOF/rGO-1, NiCo-MOF/rGO-2, and NiCo-MOF/rGO-3. From the SEM image, it was found that in NiCo-MOF/rGO-3, the density of rGO is relatively higher as the concentration of rGO utilized here is high. The SEM image confirmed that a consistent density of MOF nanosheets retaining honeycomb structures is uniformly grown on the surface of the rGO sheets. Also, the TEM images suggest that ultrathin MOF nanosheets were grown on rGO sheets. The sample bearing no rGO, *i.e.*, NiCo-MOF/rGO-O, showed a BET surface area of about 1256 m^2 g^{-1}, while the NiCo-MOF/rGO-3 sample showed a BET surface area of 580 m^2 g^{-1}. More mesopores and macropores were formed, as evident from the decrease in BET surface area in connection with rGO concentration. For all the samples, cyclic voltammetry experiments were performed, and the samples exhibited a pair of redox peaks, suggesting a pseudocapacitive property. The CV data indicated that the CV area increases with an increase in rGO precursor in the sample and later decreases as rGO increases. From the GCD curves of all the samples, it was found that a two-step discharge process occurs. Initially, the potential drops suddenly, and later it discharges slowly. During the initial discharge steps, the electrode potential comes from the electric double layer or surface charge storage as in the initial stage. Activation of the inactive electrode material is observed when the potential reaches a certain value, and the device starts to show pseudocapacitance. From the GCD data, the obtained values of specific capacitance are reported to be 968, 1100, 1553, and 1451 F g^{-1} at a current density of 1 A g^{-1} for NiCo-MOF/rGO-O, NiCo-MOF/rGO-1, NiCo-MOF/rGO-2, and NiCo-MOF/rGO-3, respectively. After 5000 charge–discharge cycles, NiCo-MOF/rGO-1, NiCo-MOF/rGO-2, and NiCo-MOF/rGO-3 exhibited 72, 83.6, and 90% capacitance retention, respectively. The increase in the rGO ratio enhances the cyclic stability, and NiCo-MOF/rGO-3 provides better cyclic stability than that of others.

Kim and co-workers prepared Ni–Co-MOF/GO *via* a one-pot solvothermal process (Fig. 15).[168] Three samples were synthesized depending on the amount of graphene oxide, namely Ni–Co-MOF/GO1, Ni–Co-MOF/GO2, and Ni–Co-MOF/GO3.

Three-electrode configurations were used to study the electrochemical property in 6 M KOH. The values of specific capacitance obtained from the GCD data were 120 and 230.9 F g^{-1} for Ni–Co-MOF and Ni–Co-MOF/GO1, respectively, at a current density of 1 A g^{-1}. Ni–Co-MOF/GO1, Ni–Co-MOF/GO2, and Ni–Co-MOF/GO3 demonstrated specific capacitances of 230.9, 447.2, and 341.8 F g^{-1} at a current density of 1 A g^{-1}. The capacitive performance of the composite electrode can be associated with the synergistic effect of M-MOF, where Co partly takes the place of nickel and graphene oxide. Graphene oxide with a 2D layer structure produces a good amount of area for intercalation and deintercalation of OH$^-$. The 3D structure of the composite gained by the synthesis of Ni–Co-MOF with the porous microstructure of the graphene oxide sheet able to assist the progress of high-speed charge transfer and the exposure of active sites to the electrolyte. This increases the capacitance value, where 99.6% reservation of capacitance value occurred for Ni–Co-MOF/GO2 after 3000 cycles.
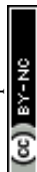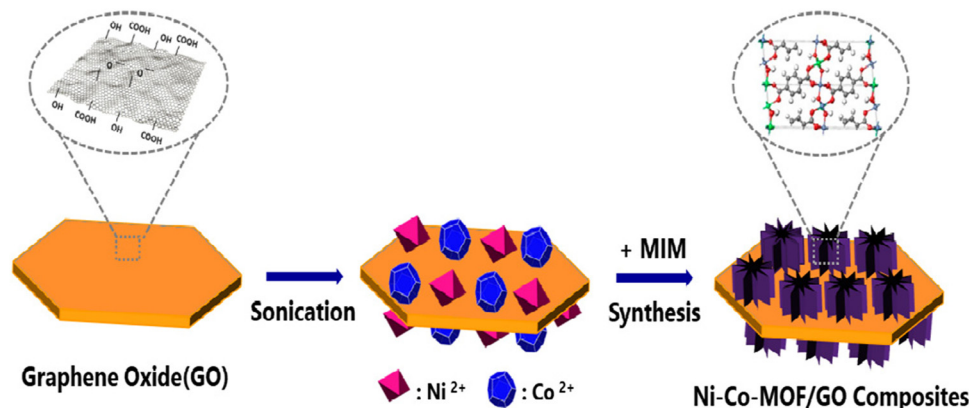
Fig. 15 The scheme for the preparation process of Ni–Co-MOF/graphene oxide composites. Reproduced from ref. 168 with permission from Elsevier Ltd, Copyright 2019.

Andikaey *et al.* synthesized another NiCo MOF *via* the solvothermal method using $Co(NO_3)_2 \cdot 6H_2O$, $Ni(NO_3)_2 \cdot 6H_2O$, and 1,4-benzene dicarboxylic acid.[169] Liquid-phase exfoliated graphene (LEG) was prepared from a natural graphite shell using a green, cheap, and facile method. van der Waals and hydrophobic forces allow the adsorption of glucose derivatives on the LEG surface, and the connection of Ni and Co precursors is possible as the –OH and –COOH groups supply the active sites. This nanocomposite exhibited a $154.9 \ m^2 \ g^{-1}$ surface area with an average pore diameter of 7.23 nm. The CV curve of the GM-LEG@NiCo-MOF electrode showed two redox peaks, which came from the redox reactions of Co(IV)/Co(III) and Ni(II)/Ni(III). The higher capacitance of GM-LEG@NiCo-MOF than NiCo-MOF or GM-LEG results from the synergistic effect of NiCo-MOF and GM-LEG in the nanocomposite. From the GCD curve, the obtained value of specific capacitance for GM-LEG@NiCo-MOF was $4077.3 \ F \ g^{-1}$. The good electrical conductivity of GM-LEG and the quasi-capacitive character of NiCo-MOF were the reasons behind the superb capacitance of GM-LEG@NiCo-MOF.

Mousavi and co-workers developed an Ni,Co-based MOF and reduced graphene oxide nanocomposite Ni/Co-MOF–rGO for use in supercapacitor applications.[170] Electrochemical measurements were conducted in a 6 M KOH solution. Ni/Co-MOF–rGO exhibited a specific capacitance of $860 \ F \ g^{-1}$ at a current density of $1 \ A \ g^{-1}$, which is higher than that of Ni/Co-MOF, Ni-MOF, or Co-MOF. The authors suggested three reasons behind the higher capacitance value: (i) the higher surface area with a smaller particle size of the Co MOF favours capacitive charge storage; (ii) efficient synergistic effects among the Ni and Co metals are possible due to the homogeneous distribution of the MOF particles in the dual Ni/Co MOF composite, resulting in better capacitance performance; and (iii) synergistic effects among the MOF and rGO can act as a current collector at a nanoscale level and support the composite. The charge transfer resistance value from the EIS measurement for the Ni/Co-MOF–rGO electrode was the lowest ($< 5 \ \Omega$) among all the materials used in this study. A two-electrode asymmetric device was assembled for real utilization. The

device delivered a specific energy of $72.8 \ W \ h \ kg^{-1}$ with a specific power of $850 \ W \ kg^{-1}$ at a current density of $1 \ A \ g^{-1}$. The asymmetric device showed 91.6% retention of capacitance value after carrying out 6000 GCD cycles. For practical application purposes, the authors tried to turn on a clock and light up blue, green, and red LEDs using this prototype device (Fig. 16).

An Ni/Co-MOF/rGO composite with spherical particles decorated with rod-like morphology was synthesized by Kumaraguru *et al.* for electrochemical supercapacitor performance.[171] Three-electrode configurations were utilized to perform electrochemical experiments on Ni/Co-MOF and Ni/Co-MOF/rGO in a 1 M KOH solution. Using the CV approach, the electrochemical activity of Ni/Co-MOF and Ni/Co-MOF/rGO composites was evaluated at various sweep rates varying from 5 to $100 \ mV \ s^{-1}$ (Fig. 17(A) and (B)). The presence of a redox peak in the CV curve indicated the pseudocapacitive nature of the Ni/Co-MOF and Ni/Co-MOF/rGO composites. At a scan rate of $5 \ mV \ s^{-1}$, Fig. 17(C) shows the CV profiles of composite electrodes made of Ni/Co-MOF and Ni/Co-MOF/rGO. Ni/Co-MOF and Ni/Co-MOF/rGO showed specific capacitances of 678 and $1162 \ F \ g^{-1}$ at a scan rate of $5 \ mV \ s^{-1}$. Specific capacitance is depicted against scan rate in Fig. 17(D), where there is an opposite correlation. The higher capacitance of Ni/Co-MOF/rGO in comparison to Ni/Co-MOF was explained by the following facts: (i) the rod-like morphology bearing high surface area helps by providing an electrical pathway for electron transport, facilitation of electron conduction, shortening of the diffusion path length of ions, and giving more pathways for ion diffusion; and (ii) the synergetic effect of rod-like Ni/Co-MOF and electronically conducting rGO furnish efficient and quick charge transfer features, boosting the overall electronic conductivity.

From the GCD data, the calculated specific capacitances of Ni/Co-MOF and Ni/CoMOF/rGO electrodes were 565 and $958 \ F \ g^{-1}$, respectively, at a current density of $1 \ A \ g^{-1}$. 109% conservation of capacitance occurred after performing 5000 cycles at a scan rate of $100 \ mV \ s^{-1}$. The higher stability was associated with two reasons: (i) enhancement in fast electron transfer over the Ni/Co-MOF rods occurs owing to the conductive network of rGO; and (ii) aggregation of the
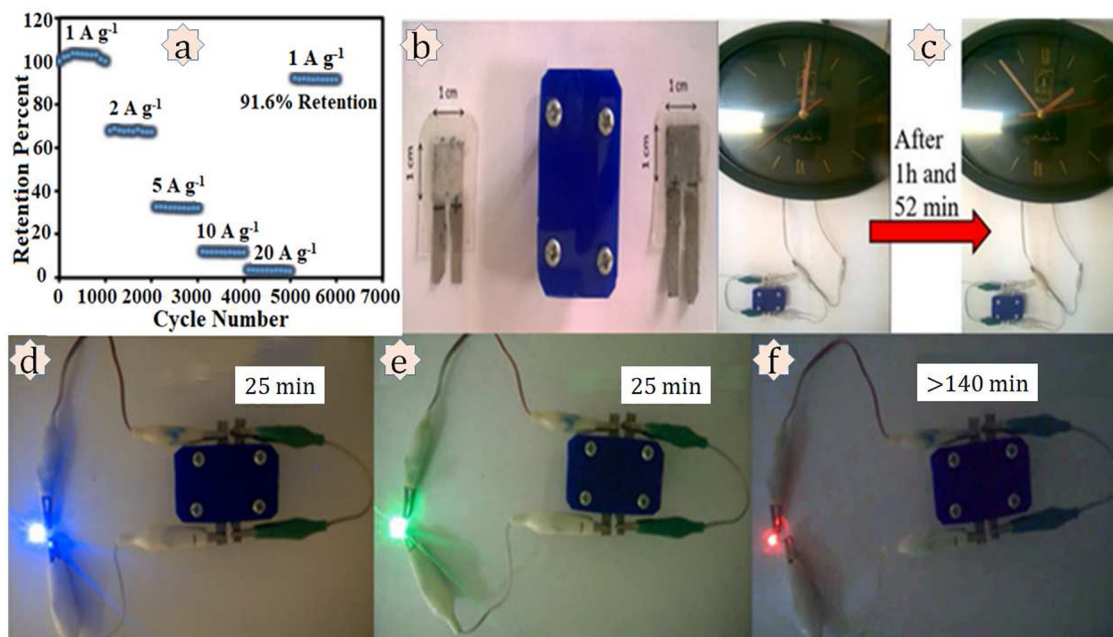
Fig. 16 Investigation of practical applications. (a) Long-term cycling stability of the AC//Ni/CoMOF−rGO device at different current densities. Practical applications of the AC//Ni/Co-MOF−rGO device: (b) a simple laboratory prototype of the fabricated device; (c) turning on a clock for 1 h and 52 min; sequential lighting up of (d) blue, (e) green, and (f) red LEDs for a definite time. Reproduced from ref. 170 with permission from Elsevier Ltd, Copyright 2018.
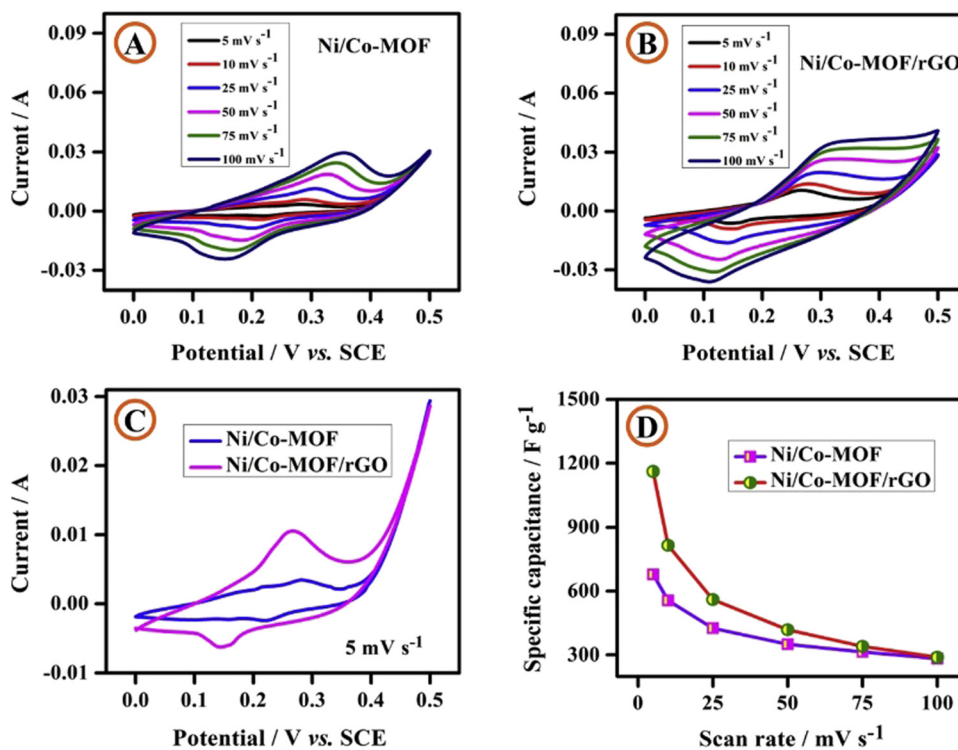

Fig. 17 Cyclic voltammetric curves of (A) Ni/Co-MOF and (B) the Ni/Co-MOF/rGO composite at various scan rates; (C) cyclic voltammetric curves of Ni/Co-MOF and the Ni/CoMOF/rGO composite at a scan rate of 5 mV s^{-1} and (D) specific capacitance *vs.* scan rate. Reproduced from ref. 171 with permission from Elsevier Ltd, Copyright 2020.

rod-like morphology of Ni/Co-MOF is prevented due to the presence of the rGO matrix, which provides ample surface area for electrochemical redox reactions.

Shi *et al.* fabricated flexible and highly conductive two-dimensional nickel cobalt MOFs/reduced graphene oxide hybrid films (2D/2D NiCo-MOFs/rGO) using a simple vacuum filtration method followed by calcination at different temperatures.[172] The authors found that the suitable ratio of MOF and graphene oxide was 2:1 as precursor materials for supercapacitor applications and denoted it as NCM/GO-2, as a higher content of NiCo-MOF resulted in the destruction of the hybrid film. Then NCM/GO-2 was treated at 200 °C, 300 °C, and 400 °C and named NCM/rGO-200, NCM/rGO-300, and NCM/rGO-400, respectively. The heat treatment process was performed to make ion diffusion feasible, resulting in the creation of active sites in the MOFs by removing the residual solvent present in them and reducing the graphene oxide to increase the conductivity of the composite material. PXRD, SEM, TEM, FTIR, Raman, BET, and XPS analyses were performed to characterize the composites. The supercapacitor performances of the synthesized materials were studied in a three-electrode arrangement using 2 M KOH as an electrolyte. The results showed that the NCM/rGO-300 hybrid film had a higher areal capacitance of 4.31 F cm^{-2} at 1 mA cm^{-2}. The higher areal capacitance NCM/rGO-300 was due to the higher conductivity and greater active sites in the MOFs of the composite material. Furthermore, an asymmetric two-electrode set-up was fabricated using NCM/rGO-300 as cathode material and activated carbon as anode material for real application. The asymmetric device achieved a higher value of areal energy density of 199.4 μW h cm^{-2} at a power density of 801.9 μW cm^{-2}. Also,

the two-electrode assembly exhibited an outstanding cyclic stability of 92.51% after 5000 cycles.

4.3.13 Co–Fe MOF–graphene composites. Safari *et al.* synthesized a bimetallic Co–Fe MOF with reduced graphene oxide of different compositions (3 and 5 wt%) on nickel foam using an ultrasonic-assisted solvothermal method.[173] The structural analysis of the synthesized composites was examined by XRD, FESEM, TEM, XPS, and BET techniques. The supercapacitor performance of the synthesized composites was carried out in a three-electrode configuration on nickel foam using 3 M KOH as an electrolyte. In the CV curves for all the electrodes, two strong peaks were detected due to the reversible redox reactions of Fe(III) ↔ Fe(II) and Co(II) ↔ Co(III). Due to the higher surface area and proper microporosity, the 3% rGO@CoFe-MOF/NF electrode showed a higher specific capacitance of 2069.1 F g^{-1} at 0.5 A g^{-1}. Also, the charge storage mechanism was well studied by the authors, which revealed the dominance of an ion-diffusion-controlled process for 3% rGO@CoFe-MOF (Fig. 18). In Fig. 18(a), the slope of the graphs is directly correlated with the diffusion coefficient, *D*. The *b*-values of 3% rGO@CoFe-MOF are approximately 0.44 and 0.41, which were associated with the reduction and oxidation reaction peaks, respectively, as shown in Fig. 18(b). According to Fig. 18(c), CoFe-MOF, 3% rGO@CoFe-MOF, and 5% rGO@CoFe-MOF, correspondingly, comprise 17, 33, and 18% of the entire area. The shaded areas of Fig. 18(d)–(f) represent surface-controlled impacts with a scan rate of 10 mV s^{-1}. A two-electrode system was fabricated by utilizing an rGO@CoFe-MOF/NF electrode as the cathode and activated carbon pasted on nickel foam as the anode material. The assembled asymmetric device possessed a higher energy

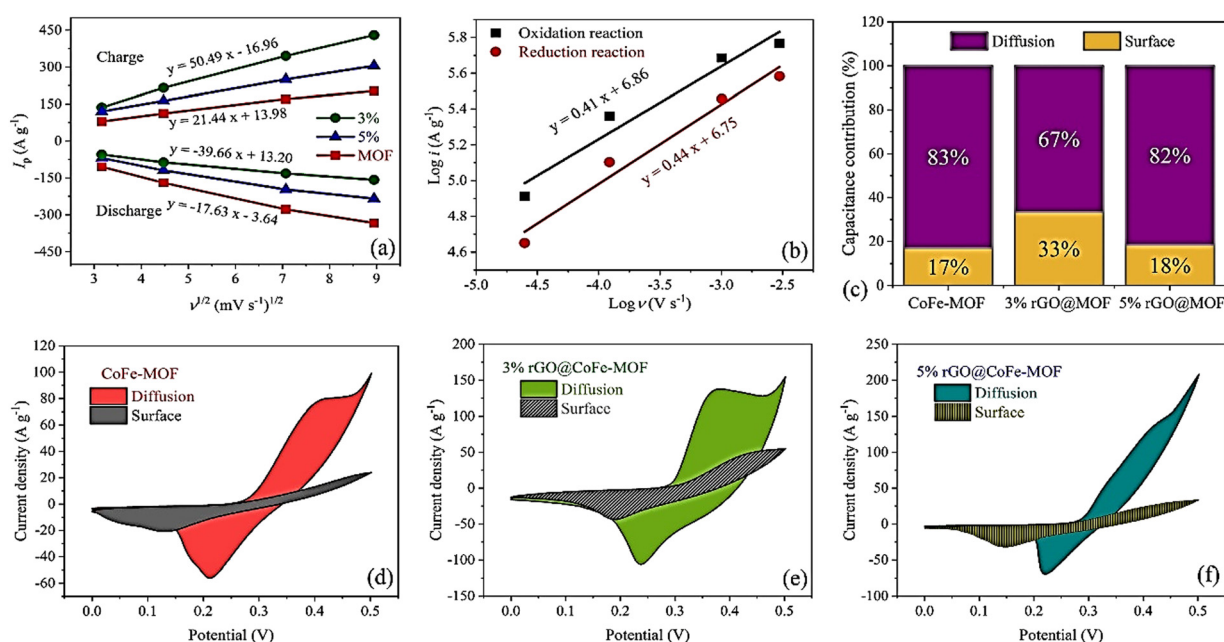**Fig. 18** (a) The curves of the peak current *versus* the square root of sweep rate (Randles–Sevcik plot). (b) The plots of log *i* versus log *ν*. (c) Capacitance contribution for three electrodes, the capacitive contribution of CV curves at 10 mV s^{-1} for (d) CoFe-MOF, (e) 3% rGO@CoFe-MOF, and (f) 5% rGO@CoFe-MOF. Reproduced from ref. 173 with permission from Elsevier Ltd, Copyright 2023.

density of 75.8 W h kg^{-1} with a power density of 700 W kg^{-1}. The cyclic stability of the assembled device was also measured, demonstrating 83.8% capacitance retention of the electrode after 10 000 cycles, suggesting the superior performance of the electrode towards energy storage devices.

4.3.14 Zn–Co MOF–graphene composites. Kıranşan and co-workers fabricated a free-standing, flexible, all-solid-state supercapacitor (FASC) using a bi-metallic ZnCo-MOF synthesized by a solvothermal method doped with a 3D-graphene sponge (GS).[174] Characterization was performed using PXRD, FTIR, Raman, SEM, EDX, and XPS analyses. The authors studied the capacitive behaviour of ZnCo-MOF/GS in 3 M KOH electrolytic solution using different electrochemical techniques. For ZnCo-MOF/GS, the specific capacitance value was calculated to be 695 F g^{-1} at 1 A g^{-1}, which is much higher than that of GS (392 F g^{-1}), which is attributed to the synergistic effect of Zn and Co, higher conductivity, and the specific rhombic dodecahedron structure of the composite. The effect of electrolytes on capacitive behaviour was studied by the authors. CV curves were carried out using three different types of electrolyte (1 M H$_2$SO$_4$, 3 M KOH, 1 M Na$_2$SO$_4$). The authors observed higher capacitance values in KOH electrolytes. This is because MOF structures oxidize in acidic electrolytes, resulting in disruption of the structures from GS, and in neutral electrolytes, the diameter of the sulfate ions is not matched with the pore structure of ZnCo-MOF/GS. For further applications in real life, a two-electrode symmetric device was fabricated, which showed a high capacitance value of 302 F g^{-1} at 1 A g^{-1}. Also, the device had an excellent high energy density of 108 W h kg^{-1} and a power density of 5037 W kg^{-1} over a large range of operating voltage (2.8 V). Additionally, the flexibility of the device was tested by bending it at different angles (90° and 180°), and it exhibited nearly the same capacitance value, indicating the high rate of flexibility and durability of the fabricated device.

4.3.15 Cu–Fe MOF–graphene composites. A CuFeBTC/S-GNS composite was prepared by Rajpurohit et al. using sulfur-doped graphene (S-GNS), benzene-1,3,5-tricarboxylic acid, and equimolar concentrations of Cu(NO$_3$)$_2$·3H$_2$O and Fe(NO$_3$)$_3$.9H$_2$O (see Scheme 4).[175]

The TEM study revealed that the surface of graphene was changed with the sulfur atoms. In CuFeBTC/S-GNS, the distinctive characteristics of CuBTC and S-GNS were finely displayed where the heavy CuFeBTC particles were routinely arranged on the surface of S-GNS. The BET-surface areas for the CuFeBTC/S-GNS composite and CuFeBTC were found to be 568.75 m^2 g^{-1} and 313.54 m^2 g^{-1}, respectively, with large pore volumes of 0.52 cm^3 g^{-1} and 0.24 cm^3 g^{-1}. The surface area of CuFeBTC increased upon the addition of S-GNS, which provides better electrochemical charge storage properties. The CuFeBTC/S-GNS composite in 1 M Na$_2$SO$_4$ exhibited a rectangular shape under the CV curve, indicating high charge storage ability. The synergy of S-GNS and CuFeBTC MOF proceeds with the EDLC charge storage mechanism from S-GNS and pseudocapacitance from the redox process in the MOF (Scheme 5). Cyclic voltammetry experiments were performed at different
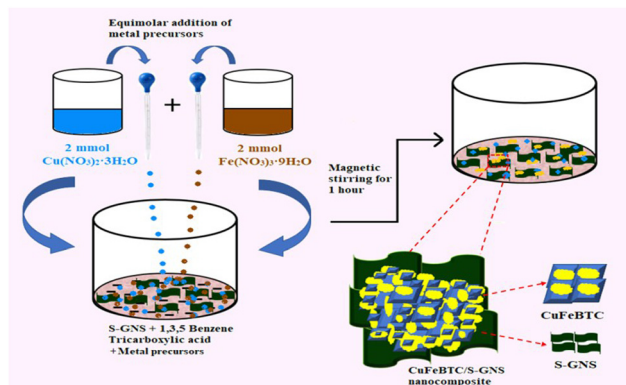
Scheme 4 Schematic illustration of the synthesis procedure of CuFeBTC/S-GNS nanocomposite. Reproduced from ref. 175 with permission from Elsevier Ltd, Copyright 2019.
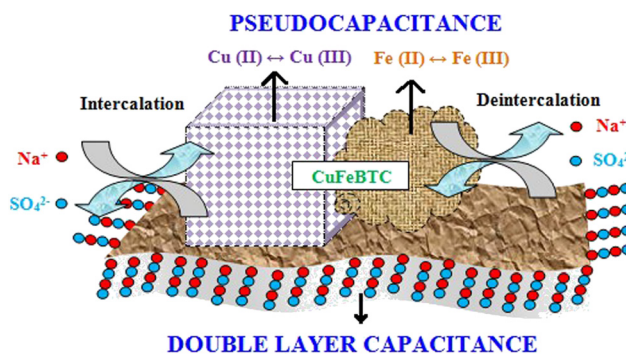
Scheme 5 Pictorial representation of charge storage in the CuFeBTC/S-GNS nanocomposite. Reproduced from ref. 175 with permission from Elsevier Ltd, Copyright 2019.

scan rates for CuFeBTC nanopowder and CuFeBTC/S-GNS nanocomposite electrodes. CuFeBTC showed two redox peaks even at a high scan rate, suggesting good reversibility in electrochemical performance and rate performance. However, in the case of CuFeBTC/S-GNS, the supercapacitor behaviour of the composite increased with increasing scan rate owing to the steep rise in specific current.

The addition of S-GNS to CuFeBTC provides maximum EDLC effect to pristine CuFeBTC, which improves its supercapacitor behaviour. From the GCD plot, the specific capacitance value was 1164.3 F g^{-1} at a current density of 0.5 A g^{-1} for CuFeBTC/S-GNS. The authors suggested some reasons behind the high specific capacitance of the hybrid composite: (i) instant contact between the CuFeBTC network and high-surface-area S-GNS sheets is possible due to the typical structure of CuFeBTC/S-GNS; (ii) the heterobimetallic structure of CuFeBTC with sufficient porosity provides high charge storage, and destruction of the heterobimetallic MOF is prevented due to the presence of S-GNS; (iii) the penetrated S-GNS sheets reveal discrete CuFeBTC particles and this connection increases the conductivity, ultimately providing efficient

transportation of charge across the structure; and (iv) electrical double layer charge storage is possible with S-GNS through the adsorption of electrolyte ions on its surface. The heterobimetallic MOF gathered on the surface of S-GNS with a tunable porous structure provides high surface area and electronic conductivity. These are the reasons behind the good supercapacitance performance. An improvement in electrochemical kinetics is possible as the interconnected structure allows swift electron and electrolyte transport at the time of the charge–discharge process. This interconnected structure permits electrolyte transport and swift electrons during the charge–discharge process, enhancing the electrochemical kinetics. The cycle life of CuFeBTC and CuFeBTC/S-GNS electrodes was measured by collecting consecutive GCD cycles at 0.5 A g^{-1}, where 90.2% and 79.4% retention of initial capacitance occurred after 4500 cycles for CuFeBTC/S-GNS and CuFeBTC, respectively. To apply CuFeBTC/S-GNS in a real application, a two-electrode symmetric supercapacitor device was assembled using CuFeBTC/S-GNS as cathode and anode.

A summary of supercapacitor performance using MOF–graphene composite is provided in Table 1.

4.4 Various Other MOF-based composites and their derivatives

For an improvement in the conductivity issue, several other MOF-based composites and their derivatives were prepared and utilized for supercapacitor purposes. In composites, synergistic effects between two interconnected materials can be employed to maximize the benefits of single materials or to get around their drawbacks.[176] Thus, one may create hybrid electrodes for applications involving supercapacitors using the composite construction technique. The EDLC and pseudocapacitive characteristics of the relevant individual substances can be retained *via* hybrid electrodes. This hybrid approach contributes to the delivery of exceptional specific capacitance, a prolonged lifespan, good energy, and high power densities. Compared to pure MOFs, MOF derivatives not only substantially maintain their primary porous framework architecture but also display enhanced stability, a void distribution that is tunable, and sufficient electroactive locations where energy-related technology may be developed.[177] A detailed review of MOF-MXene composites and their derivatives with respect to electrochemical applications has been provided by Pang and coworkers.[177]

Table 1 A summary of supercapacitor performance using a MOF–graphene composite

Composite	Electrolyte	Specific capacitance ($F\ g^{-1}$)	Scan rate/current density	Energy density ($W\ h\ kg^{-1}$)	Power density ($W\ kg^{-1}$)	Ref.
ZIF-67/rGO	0.2 M $K_3[Fe(CN)_6]$ in 1 M Na_2SO_4	1453	4.5 A g^{-1}	25.5	2700	141
ZIF-67/GO-2	6 M KOH	100.47	5 mV s^{-1}	—	—	142
CoMG5	6 M KOH	549.96	10 mV s^{-1}	8.10	850	143
CoBTC/GNS	1 M KOH	608.2	0.25 A g^{-1}	49.8	1025.8	144
G@Ni-MOF	6 M KOH	1017	10 mV s^{-1}	39.43	34.29	145
Ni-MOF/rGO-300	6 M KOH	954	1 A g^{-1}	17.13	750	146
GM-LEG@Ni-MOF	3 M KOH	987.6	0.5 A g^{-1}	32.7	750	147
Ni-MOF/rGO	6 M KOH	1154.4	0.66 A g^{-1}	0.82	20	148
Ni-BPDC/GO-3	6 M KOH	630	1 A g^{-1}	16.5	250	149
IITKGP-20A-GO3	6 M KOH	~840	2 A g^{-1}	30.7	388.5	150
Ni-BTC@GO 2	3 M KOH	1199	1 A g^{-1}	40.89	800	151
Ni-MOF–graphene nanocomposite	2 M NaCl	111.68	0.3 A g^{-1}	14.68	291.82	152
Cu-MOF/G	6 M KOH	482	10 mV s^{-1}	34.5	1350	153
HMRL-1/R	1 M Na_2SO_4	366.6	1 A g^{-1}	14.66	21 100	154
q-2D-MOF/rGO	1 M H_2SO_4	292	1 A g^{-1}	—	—	155
MrGO	1 M KCl	208.9	—	31.2	656.4	156
Cu-MOF/rGO (**CR**)	1 M Na_2SO_4	867.09	1 A g^{-1}	30.56	12 000	157
10 wt% rGO and HKUST-1	0.5 M Na_2SO_4	385	1 A g^{-1}	42	3100	158
GAMOF(Fe^{3+})	1 M H_2SO_4	353	20 A g^{-1}	36	588	159
Zn-MOF–rGO	3 M KOH	205 C g^{-1}	1 A g^{-1}	7.1	400	160
ZIF-8/GO	6 M KOH	160	5 mV s^{-1}	—	—	161
GA@UiO-66-NH_2	1 M Na_2SO_4	651	2 A g^{-1}	73	16 000	162
MIL-53(Al)@rGO	1 M KOH	280	0.5 A g^{-1}	6.66	200	163
N-ZIF-67·rGO/NF	2 M KOH	962	20 mA cm^{-2}	—	—	164
MOF-5 Ni50%rGO50%	1 M KOH	758	—	37.8	226.7	165
MIL-101(Cr,Mg)/rGO	6 M KOH	261.41	1 A g^{-1}	4.65	7653	166
NiCo-MOF/rGO-2	—	1553	1 A g^{-1}	44	3168	167
Ni–Co-MOF/GO2	6 M KOH	447.2	1 A g^{-1}	—	—	168
GM-LEG@NiCo-MOF	Mixture of 3 M aqueous KOH and 0.1 M $K_4Fe(CN)_6$	4077.3	2.5 A g^{-1}	76.3	2250	169
Ni/Co-MOF–rGO	6 M KOH	860	1 A g^{-1}	72.8	850	170
Ni/Co-MOF/rGO	1 M KOH	1162	5 mV s^{-1}	—	—	171
2D/2D NiCo-MOFs/rGO	2 M KOH	4.31 F cm^{-2}	1 mA cm^{-2}	199.4 µW h cm^{-2}	801.9 µW cm^{-2}	172
rGO@CoFe-MOF	3 M KOH	2069.1	0.5 A g^{-1}	75.8	700	173
ZnCo-MOF/GS	3 M KOH	695	1 A g^{-1}	108	5037	174
CuFeBTC/S-GNS	1 M Na_2SO_4	1164.3	0.5 A g^{-1}	96.57	1595.12	175

The quick transfer of electrons and ions could be efficiently accelerated by the proposed hierarchical arrangement, conductive support, high active area, and enhanced interlayer spacing of MXene/MOF hybrids and their derivatives. Additionally, the interfacial contacts generated in the composites increased their chemical durability and reduced volume growth during the quick charge–discharge mechanism. Hybridization with MXene in the 3D porous structure has been studied for a high-performance asymmetric supercapacitor device using Ni-based MOF [Ni(Tdc)(Bpy)]$_n$ with a porous framework and good structural durability.[178] Rapid ion transport was made possible by the incorporation of Ni-MOF since it considerably enhanced the interlamellar gap of MXene. A highly stable Ni-Bpy linear chain may be responsible for the improved cycling stability of MXene@Ni-MOF. Compared to the electrochemical performance of MXene, MXene + Ni-MOF, and pure MOF, MXene@Ni-MOF displayed noticeably increased electrochemical performance. The presence of a highly stable Ni-Bpy linear chain was responsible for the remarkable cyclic performance of the built ASC device, with 98% retention of specific capacitance after 5000 cycles. Hierarchical nickel phosphates-MXene (MXene/NPO) were made by phosphorylating an Ni-BDC/MXene composite in a KH_2PO_4 aqueous solution for electrode materials in supercapacitor applications.[179] The electrode materials exhibited exceptional cycling stability, with 85% retention of capacity after 10 000 cycles and a high specific capacity of 639 C g^{-1} at 0.5 A g^{-1}. The nickel phosphate-derived *in situ* MOFs were decorated, strengthening the bonds between MXene and nickel phosphate and encouraging electron transport. Luo *et al.* prepared a $Co_3S_4/Ti_3C_2T_x$ composite through the sulfidation of a cobalt-based ZIF-67/$Ti_3C_2T_x$ composite in the presence of thioacetamide (TAA) under hydrothermal conditions.[180] In a 3 M KOH solution, an electrode with $Co_3S_4/Ti_3C_2T_x$ as its active substance had a very high specific capacitance of 602 F g^{-1} at a current density of 1 A g^{-1}, which was 2.6 times greater than that of an electrode with ZIF-67/$Ti_3C_2T_x$ and 4.5 times higher than that of electrodes with ZIF-67. At 10 A g^{-1}, $Co_3S_4/Ti_3C_2T_x$ exhibited 81.6% retention of capacitance, which was larger than those of ZIF-67 of 67.7% or ZIF-67/$Ti_3C_2T_x$ of 75.8%. The authors suggested that the greater effectiveness of the Co_3S_4/Ti_3C_2Tx-based electrode can be attributed to (1) its greater reactivity and pseudocapacitance, which, when combined with (2) its substantial porosity, are very helpful for the quick insertion–extraction of OH$^-$ from the electrolyte. (3) The third component is a three-dimensional (3D) structure that offers simple conductive routes for effective transport of charges and electrolyte infiltration. (4) The final, but certainly not least reason is the existence of $Ti_3C_2T_x$, which offered stability and support to the composite and protected the entire structure from harm caused by the ongoing electrochemical processes between oxidation and reduction. The $Co_3S_4/Ti_3C_2T_x$-based electrode performed excellently in terms of rate thanks to every one of these features. MOF–carbon nanotube (CNT) composites have also been explored by many researchers.[181] Ni-MOF was directly grown on the surface of CNTs by Wang and coworkers to create Ni-MOF@CNT.[182]

Ni-MOF@CNTs provided a specific capacitance of 1765 F g^{-1} at 0.5 A g^{-1} in 6 M KOH, which was 1.6 times the capacitance of 1080 F g^{-1} for pure Ni-MOF. Furthermore, 95% of the capacitance was present in Ni-MOF@CNT after 5000 charge–discharge cycles. This dominance is due to the synergistic interaction between Ni-MOF and CNTs. The porous structure of Ni MOF can facilitate the entrance of electrolytes, while CNT may substantially boost the conductivity of the entire composite capacitor. MOF–conductive polymer composites have also been applied for supercapacitor applications. Neisi *et al.* prepared PANI/Cu-MOF at room temperature to study its supercapacitor behaviour.[183] In 6 M KOH electrolyte, with a scan rate of 5 mV s^{-1}, the composite displayed pseudocapacitance behaviour, and its specific capacitance (734 F g^{-1}) was larger than that of pure Cu-MOF of 558 F g^{-1}. By supplying ion channels and electron transport pathways, polyaniline is thought to enhance the number of sites for activity in the redox procedure, enhancing the specific capacitance. So, creating Cu-MOF hybrids with polyaniline as the polymer that conducts electricity is a successful way to raise the specific capacitance and cycle life of Cu-MOF. An $Ni_3(NO_3)_2(OH)_4$@ZrMOF composite with a flower-like morphology was prepared by Tang and coworkers to study its supercapacitor performance.[184] In 6 M KOH, $Ni_3(NO_3)_2(OH)_4$@ZrMOF displayed a higher specific capacitance of 992 F g^{-1} at a scan rate of 5 mV s^{-1} compared to 134 F g^{-1} for Zr-MOF and 753 F g^{-1} for $Ni_3(NO_3)_2(OH)_4$. After 3000 cycles, the $Ni_3(NO_3)_2(OH)_4$@ZrMOF electrode showed outstanding capacitance retention, suggesting good cycling stability. The large specific surface area of Zr-MOF, which maximizes $Ni_3(NO_3)_2(OH)_4$ dispersion on Zr-MOF, is credited for the high specific capacitance. Additionally, the porous structure of Zr-MOF offers ions easy paths to travel. Yao *et al.* prepared a $K_{0.5}Mn_2O_4$@Mn-MOF-8 nanosheet array composite to perform a supercapacitor study.[185] $K_{0.5}Mn_2O_4$@Mn-MOF-8 exhibited a remarkable capacitance of 886.9 F g^{-1} at 1 A g^{-1} current density. The asymmetric device (ASC) comprised $K_{0.5}Mn_2O_4$@Mn-MOF-8 and WO_3, which had a potential window of 2 V and remarkable cycling stability. The authors suggested three reasons for the better performance of $K_{0.5}Mn_2O_4$@Mn-MOF-8. First, by adding or removing the hydrated cations (K$^+$) of $K_{0.5}Mn_2O_4$, the conductivity of the electrode materials is improved, and the capacitance is increased. Also, the synergistic as well as annealing effect of various metals are the driving forces to enhance the electrochemical performance towards supercapacitor applications.[186–188] In the electrochemical examination, the added crystal water supports a stable structure and inhibits the dissolution of manganese oxide. Second, $K_{0.5}Mn_2O_4$ nanosheets with a vertical orientation and an interlayer spacing of 7.2 Å offer a large number of places for the storage of electrolyte ions and improve the efficiency of electrolyte uptake on the electrochemical interface. Third, the contact surface of the vertically co-oriented $K_{0.5}Mn_2O_4$@Mn-MOF-8 nanosheets enhances the utilization rate of the electrode material and contains a large number of active sites.

5 Conclusions and future perspectives

In this review article, we have discussed the synthesis of different kinds of MOF–graphene composites and explored them in supercapacitor applications. Different types of transition-metal-based MOFs have been discussed with MOF–graphene composites in the field of supercapacitor application with their working principles. Recently, MOFs have been suffering from conductivity issues in their pristine form, so this limitation will be improved through the development of MOF–graphene composites. The mechanisms of supercapacitor behaviour using different metal-based MOF–graphene composites have also been addressed. The benefit of using a MOF–graphene composite compared to a pure MOF has been well explained. The exploration, emerging applications, key challenges, and future perspectives of MOF–graphene composites have been demonstrated in Fig. 19.

Despite significant advances in the research and development of MOF–graphene composite-based supercapacitor electrode materials, there are still a number of obstacles to be overcome before supercapacitors based on this technology may be commercialized with these resources. The following are the difficulties:

Fig. 19 The exploration, emerging applications, key challenges, and future perspective of MOF–graphene composites.

(a) For exceptionally well-suited applications, it is crucial to reduce the size of MOFs on graphene in order to provide additional active regions for effective electrochemical reactions while avoiding agglomeration.

(b) Currently, there are just a few reported varieties of MOFs, mostly from the ZIF, MIL, UiO, and HKUST-1 series. More optimized MOFs and their graphene composites can be produced by carefully controlling their makeup and composition.

(c) In addition to significantly impacting charge transfer, the strength of the surface among MOFs and graphene also influences ion adsorption energy and diffusion kinetics, which in turn affects supercapacitor efficiency.

(d) MOF–graphene composites need to work in severe environments and function at their peak under particular circumstances (pH, temperature, humidity, *etc.*) for supercapacitor applications; their potential for advancement is somewhat constrained.

(e) Despite the fact that the materials used in electrodes made of MOF–graphene composites exhibit favourable properties, it is unclear exactly how these structural modifications and their effects on the electrochemical process work. It is essential to understand the electrochemical activities for designing high-performance electrode materials.

(f) The biggest issue with the broad acceptance of MOF–graphene composite electrodes is expense. Using expensive ligands, solvents, and laborious preparation methods has made massive production difficult in several ways.

Even though MOF–graphene composites face the aforementioned difficulties, the following modifications could be made to address these problems and enhance the supercapacitor performance of MOF–graphene composites.

(a) To create these incredibly small-sized MOFs, a novel and efficient method of synthesis must be developed.

(b) Additional MOF-based functional materials, like conductive MOFs, may be advantageous for electrochemical applications. Besides that, certain MOFs with excellent conductivity, chemical, thermal, and mechanical stability may be used in combination with graphene to create composites.

(c) Developing materials that use MOF–graphene composites with strong interfacial interactions thus becomes crucial for improving supercapacitor efficiency.

(d) In this respect, MOF–graphene composites still have opportunities for advancement. By using highly charged metal ions with oxygen donor sites of carboxylate ligands, a viable dual-ligand method can be constructed to improve building unit connections, enhance the framework hydrophobicity, and increase the rigidity of ligand-stable MOFs. Besides that, post-synthetic modifications (PSMs) could be undertaken to substitute the labile components with stable ones, increasing the stability of the framework.

(e) Extensive studies are required using experimental measurements, theoretical calculations, and simulation studies with the objective of learning more about the electrochemical mechanism of a supercapacitor. Furthermore, sophisticated characterization tools are also necessary.

(f) It is vitally necessary to develop innovative kinds of synthetic techniques in order to streamline the process and

improve the uniformity of the composites that are produced. Large-scale manufacturing of MOFs and MOF–graphene composites could be made feasible at a relatively low cost due to the discovery of a range of straightforward and efficient methods of synthesis, like the one-pot solvent approach.

In conclusion, MOF–graphene composite materials have the potential for the extension of the usage of MOF-based materials despite the fact that there remain some obstacles to be overcome. We think that the information presented in this review will be useful for gaining an insight into how MOF–graphene composites are being used as potential materials in the area of supercapacitors and will serve as a useful resource for further investigation.

Abbreviations

ZIF	Zeolitic imidazolate framework
G	Graphene
MIL	Materials Institute Lavoisier
UiO	Universitetet i Oslo

Conflicts of interest

There are no conflicts to declare.

Acknowledgements

References

1 X. Mu, H. Pan, P. He and H. Zhou, *Adv. Mater.*, 2020, **32**, 1903790.
2 S. Liu, L. Kang and S. C. Jun, *Adv. Mater.*, 2021, **33**, 2004689.
3 Y. Cao, J. Liang, X. Li, L. Yue, Q. Liu, S. Lu, A. M. Asiri, J. Hu, Y. Luo and X. Sun, *Chem. Commun.*, 2021, **57**, 2343.
4 S. Zheng, H. Xue and H. Pang, *Coord. Chem. Rev.*, 2018, **373**, 2.
5 D. P. Dubal, P. Gomez-Romero, B. R. Sankapal and R. Holze, *Nano Energy*, 2015, **11**, 377.
6 D. P. Dubal, J. G. Kim, Y. Kim, R. Holze, C. D. Lokhande and W. B. Kim, *Energy Technol.*, 2014, **2**, 325.
7 A. Agarwal and B. R. Sankapal, *J. Mater. Chem. A*, 2021, **9**, 20241.
8 S. Liang, H. Wang, Y. Li, H. Qin, Z. Luo, B. Huang, X. Zhao, C. Zhao and L. Chen, *Sustainable Energy Fuels*, 2020, **4**, 3825.

9 T. Guo, D. Zhou, L. Pang, S. Sun, T. Zhou and J. Su, *Small*, 2022, **18**, 2106360.
10 C. Zhong, Y. Deng, W. Hu, J. Qiao, L. Zhang and J. Zhang, *Chem. Soc. Rev.*, 2015, **44**, 7484.
11 L. Wang, Y. Han, X. Feng, J. Zhou, P. Qi and B. Wang, *Coord. Chem. Rev.*, 2016, **307**, 361.
12 M. Rajkumar, C.-T. Hsu, T.-H. Wu, M.-G. Chen and C.-C. Hu, *Prog. Nat. Sci.: Mater. Int.*, 2015, **25**, 527.
13 I. Hussain, C. Lamiel, M. Ahmad, Y. Chen, S. Shuang, M. S. Javed, Y. Yang and K. Zhang, *J. Energy Storage*, 2021, **44**, 103405.
14 Y. Zeng, M. Yu, Y. Meng, P. Fang, X. Lu and Y. Tong, *Adv. Energy Mater.*, 2016, **6**, 1601053.
15 S. Liu, L. Kang, J. Henzie, J. Zhang, J. Ha, M. A. Amin, M. S. A. Hossain, S. C. Jun and Y. Yamauchi, *ACS Nano*, 2021, **15**, 18931.
16 Z. Yang, J. Tian, Z. Yin, C. Cui, W. Qian and F. Wei, *Carbon*, 2019, **141**, 467.
17 S. Kumar, G. Saeed, L. Zhu, K. N. Hui, N. H. Kim and J. H. Lee, *Chem. Eng. J.*, 2021, **403**, 126352.
18 Z. Yu, L. Tetard, L. Zhai and J. Thomas, *Energy Environ. Sci.*, 2015, **8**, 702.
19 J. Huang, K. Yuan and Y. Chen, *Adv. Funct. Mater.*, 2022, **32**, 2108107.
20 J. Yan, Q. Wang, T. Wei and Z. Fan, *Adv. Energy Mater.*, 2014, **4**, 1300816.
21 A. Velasco, Y. K. Ryu, A. Boscá, A. Ladrón-de-Guevara, E. Hunt, J. Zuo, J. Pedrós, F. Calle and J. Martinez, *Sustainable Energy Fuels*, 2021, **5**, 1235.
22 C. Yuan, L. Yang, L. Hou, L. Shen, X. Zhang and X. W. Lou, *Energy Environ. Sci.*, 2012, **5**, 7883.
23 Y. Zhu, S. Murali, M. D. Stoller, K. J. Ganesh, W. Cai, P. J. Ferreira, A. Pirkle, R. M. Wallace, K. A. Cychosz, M. Thommes, D. Su, E. A. Stach and R. S. Ruoff, *Science*, 2011, **332**, 1537.
24 M. Winter and R. J. Brodd, *Chem. Rev.*, 2004, **104**, 4245.
25 X. Yang, C. Cheng, Y. Wang, L. Qiu and D. Li, *Science*, 2013, **341**, 534.
26 L. L. Zhang and X. S. Zhao, *Chem. Soc. Rev.*, 2009, **38**, 2520.
27 P.-C. Chen, G. Shen, Y. Shi, H. Chen and C. Zhou, *ACS Nano*, 2010, **4**, 4403.
28 A. Burke, *J. Power Sources*, 2000, **91**, 37.
29 S. Liu, L. Kang, J. Hu, E. Jung, J. Henzie, A. Alowasheeir, J. Zhang, L. Miao, Y. Yamauchi and S. C. Jun, *Small*, 2022, **18**, 2104507.
30 J. Yang, P. Xiong, C. Zheng, H. Qiu and M. Wei, *J. Mater. Chem. A*, 2014, **2**, 16640.
31 A. S. Aricò, P. Bruce, B. Scrosati, J.-M. Tarascon and W. van Schalkwijk, *Nat. Mater.*, 2005, **4**, 366.
32 V. Subramanian, H. Zhu, R. Vajtai, P. M. Ajayan and B. Wei, *J. Phys. Chem. B*, 2005, **109**, 20207.
33 S. Sarangapani, B. V. Tilak and C. P. Chen, *J. Electrochem. Soc.*, 1996, **143**, 3791.
34 S. Sanati, R. Abazari, A. Morsali, A. M. Kirillov, P. C. Junk and J. Wang, *Inorg. Chem.*, 2019, **58**, 16100.
35 R. Zeng, Z. Li, L. Li, Y. Li, J. Huang, Y. Xiao, K. Yuan and Y. Chen, *ACS Sustainable Chem. Eng.*, 2019, **7**, 11540.

36 M. Yi, C. Zhang, C. Cao, C. Xu, B. Sa, D. Cai and H. Zhan, *Inorg. Chem.*, 2019, **58**, 3916.

37 A. Mohanty, D. Jaihindh, Y.-P. Fu, S. P. Senanayak, L. S. Mende and A. Ramadoss, *J. Power Sources*, 2021, **488**, 229444.

38 Z. Sun, K. Qu, Y. You, Z. Huang, S. Liu, J. Li, Q. Hu and Z. Guo, *J. Mater. Chem. A*, 2021, **9**, 7278.

39 N. H. N. Azman, M. S. M. Mat Nazir, L. H. Ngee and Y. Sulaiman, *Int. J. Energy Res.*, 2018, **42**, 2104.

40 Y. Huang, H. Li, Z. Wang, M. Zhu, Z. Pei, Q. Xue, Y. Huang and C. Zhi, *Nano Energy*, 2016, **22**, 422.

41 M. Sajjad, M. I. Khan, F. Cheng and W. Lu, *J. Energy Storage*, 2021, **40**, 102729.

42 Q. Yang, Z. Li, R. Zhang, L. Zhou, M. Shao and M. Wei, *Nano Energy*, 2017, **41**, 408.

43 D. Pech, M. Brunet, H. Durou, P. Huang, V. Mochalin, Y. Gogotsi, P.-L. Taberna and P. Simon, *Nat. Nanotechnol.*, 2010, **5**, 651.

44 X. Chu, F. Meng, T. Deng and W. Zhang, *Nanoscale*, 2021, **13**, 5570.

45 S. Liu, L. Kang, J. Zhang, S. C. Jun and Y. Yamauchi, *NPG Asia Mater.*, 2023, **15**, 9.

46 S. Liu, D. Ni, H.-F. Li, K. N. Hui, C.-Y. Ouyang and S. C. Jun, *J. Mater. Chem. A*, 2018, **6**, 10674.

47 S. Liu, L. Kang, J. Zhang, E. Jung, S. Lee and S. C. Jun, *Energy Storage Mater.*, 2020, **32**, 167.

48 M. Kandasamy, S. Sahoo, S. K. Nayak, B. Chakraborty and C. S. Rout, *J. Mater. Chem. A*, 2021, **9**, 17643.

49 Y. Liu, Q. Wu, L. Liu, P. Manasa, L. Kang and F. Ran, *J. Mater. Chem. A*, 2020, **8**, 8218.

50 N. Kumar, L. Pradhan and B. K. Jena, *Wiley Interdiscip. Rev.: Energy Environ.*, 2022, **11**, e415.

51 S. Kamila, P. Mane, R. I. Mohanty, B. Chakraborty and B. K. Jena, *Electrochim. Acta*, 2021, **399**, 139357.

52 B. Mohanty, L. Giri and B. K. Jena, *Energy Fuels*, 2021, **35**, 14304.

53 S. K. Das, S. Kamila, B. Satpati, M. Kandasamy, B. Chakraborty, S. Basu and B. K. Jena, *J. Power Sources*, 2020, **471**, 228465.

54 S. Kamila, M. Kandasamy, B. Chakraborty and B. K. Jena, *New J. Chem.*, 2020, **44**, 1418.

55 S. Kamila, B. Chakraborty, S. Basu and B. K. Jena, *J. Phys. Chem. C*, 2019, **123**, 24280.

56 S. Kamila, B. K. Jena and S. Basu, *Energy Storage*, 2021, p. 119, DOI: 10.1002/9781119555599.ch4.

57 L. L. Zhang, R. Zhou and X. S. Zhao, *J. Mater. Chem.*, 2010, **20**, 5983.

58 Y. B. Tan and J.-M. Lee, *J. Mater. Chem. A*, 2013, **1**, 14814.

59 C. Pei, M. S. Choi, X. Yu, H. Xue, B. Y. Xia and H. S. Park, *J. Mater. Chem. A*, 2021, **9**, 8832.

60 Z. Bi, Q. Kong, Y. Cao, G. Sun, F. Su, X. Wei, X. Li, A. Ahmad, L. Xie and C.-M. Chen, *J. Mater. Chem. A*, 2019, **7**, 16028.

61 D. Ghosh, A. Pal, D. K. Singha, S. Ghosh, O. I. Lebedev, M. M. Seikh and P. Mahata, *ACS Appl. Nano Mater.*, 2020, **3**, 10105.

62 L. Li, F. Lu, R. Xue, B. Ma, Q. Li, N. Wu, H. Liu, W. Yao, H. Guo and W. Yang, *ACS Appl. Mater. Interfaces*, 2019, **11**, 26355.

63 A. Halder, M. Ghosh, A. Khayum M, S. Bera, M. Addicoat, H. S. Sasmal, S. Karak, S. Kurungot and R. Banerjee, *J. Am. Chem. Soc.*, 2018, **140**, 10941.

64 L. Pradhan, B. Nayak, A. Mukherjee, S. Basu, P. Bhanja and B. K. Jena, *ACS Appl. Energy Mater.*, 2023, **6**, 3347.

65 S. K. Das, L. Pradhan, B. K. Jena and S. Basu, *Carbon*, 2023, **201**, 49.

66 A. K. Samantara, S. Chandra Sahu, A. Ghosh and B. K. Jena, *J. Mater. Chem. A*, 2015, **3**, 16961.

67 O. M. Yaghi and H. Li, *J. Am. Chem. Soc.*, 1995, **117**, 10401.

68 H. Li, M. Eddaoudi, M. O'Keeffe and M. Yaghi, *Nature*, 1999, **402**, 276.

69 M. Li, D. Li, M. O'Keeffe and O. M. Yaghi, *Chem. Rev.*, 2014, **114**, 1343.

70 M. O'Keeffe and O. M. Yaghi, *Chem. Rev.*, 2012, **112**, 675.

71 T. R. Cook, Y.-R. Zheng and P. J. Stang, *Chem. Rev.*, 2013, **113**, 734.

72 T. Chen, F. Wang, S. Cao, Y. Bai, S. Zheng, W. Li, S. Zhang, S.-X. Hu and H. Pang, *Adv. Mater.*, 2022, **34**, 2201779.

73 D. K. Singha, P. Majee, S. K. Mondal and P. Mahata, *RSC Adv.*, 2015, **5**, 102076.

74 B. Xu, H. Zhang, H. Mei and D. Sun, *Coord. Chem. Rev.*, 2020, **420**, 213438.

75 Y. Zhao, J. Liu, M. Horn, N. Motta, M. Hu and Y. Li, *Sci. China Mater.*, 2018, **61**, 159.

76 H. Zhou, G. Zhu, S. Dong, P. Liu, Y. Lu, Z. Zhou, S. Cao, Y. Zhang and H. Pang, *Adv. Mater.*, 2023, **35**, 2211523.

77 C. Liu, Y. Bai, W. Li, F. Yang, G. Zhang and H. Pang, *Angew. Chem., Int. Ed.*, 2022, **61**, e202116282.

78 Y. Zheng, S. Zheng, H. Xue and H. Pang, *Adv. Funct. Mater.*, 2018, **28**, 1804950.

79 H.-j Qu, L.-j Huang, Z.-y Han, Y.-x Wang, Z.-j Zhang, Y. Wang, Q.-r Chang, N. Wei, M. J. Kipper and J.-g Tang, *J. Porous Mater.*, 2021, **28**, 1837.

80 Z. Wang, J. Huang, J. Mao, Q. Guo, Z. Chen and Y. Lai, *J. Mater. Chem. A*, 2020, **8**, 2934.

81 X. Zhang, S. Zhang, Y. Tang, X. Huang and H. Pang, *Composites, Part B*, 2022, **230**, 109532.

82 K. Jayaramulu, S. Mukherjee, D. M. Morales, D. P. Dubal, A. K. Nanjundan, A. Schneemann, J. Masa, S. Kment, W. Schuhmann, M. Otyepka, R. Zbořil and R. A. Fischer, *Chem. Rev.*, 2022, **122**, 17241.

83 Y. Ren and Y. Xu, *Chem. Commun.*, 2023, **59**, 6475.

84 V. Kumari, P. Pal Singh and S. Kaushal, *Polyhedron*, 2022, **214**, 115645.

85 L. Liu, Z. Niu and J. Chen, *Chem. Soc. Rev.*, 2016, **45**, 4340.

86 A. G. Pandolfo and A. F. Hollenkamp, *J. Power Sources*, 2006, **157**, 11.

87 P. Sharma and T. S. Bhatti, *Energy Convers. Manage.*, 2010, **51**, 2901.

88 Y. Bai, C. Liu, T. Chen, W. Li, S. Zheng, Y. Pi, Y. Luo and H. Pang, *Angew. Chem., Int. Ed.*, 2021, **60**, 25318.

89 Q. Ke and J. Wang, *J. Materiomics*, 2016, **2**, 37.

90 W. Shi, J. Zhu, D. H. Sim, Y. Y. Tay, Z. Lu, X. Zhang, Y. Sharma, M. Srinivasan, H. Zhang, H. H. Hng and Q. Yan, *J. Mater. Chem.*, 2011, **21**, 3422.

91 M. Lu, F. Beguin and E. Frackowiak, *Supercapacitors: Materials, Systems, and Applications*, Wiley, 2013.

92 M. S. Halper and J. C. Ellenbogen, *Supercapacitors: A Brief Overview*, The MITRE Corporation, McLean, 2006.

93 B. Garai, A. Mallick and R. Banerjee, *Chem. Sci.*, 2016, **7**, 2195.

94 M. S. Deenadayalan, N. Sharma, P. K. Verma and C. M. Nagaraja, *Inorg. Chem.*, 2016, **55**, 5320.

95 H. Kim, S. Yang, S. R. Rao, S. Narayanan, E. A. Kapustin, H. Furukawa, A. S. Umans, O. M. Yaghi and E. N. Wang, *Science*, 2017, **356**, 430.

96 P. Mahata, S. Natarajan, P. Panissod and M. Drillon, *J. Am. Chem. Soc.*, 2009, **131**, 10140.

97 P. Ramaswamy, N. E. Wong and G. K. H. Shimizu, *Chem. Soc. Rev.*, 2014, **43**, 5913.

98 P. Ji, K. Manna, Z. Lin, A. Urban, F. X. Greene, G. Lan and W. Lin, *J. Am. Chem. Soc.*, 2016, **138**, 12234.

99 C. He, D. Liu and W. Lin, *Chem. Rev.*, 2015, **115**, 11079.

100 L. J. Murray, M. Dinca and J. R. Long, *Chem. Soc. Rev.*, 2009, **38**, 1294.

101 J.-R. Li, R. J. Kuppler and H.-C. Zhou, *Chem. Soc. Rev.*, 2009, **38**, 1477.

102 R. Banerjee, A. Phan, B. Wang, C. Knobler, H. Furukawa, M. O'Keeffe and O. M. Yaghi, *Science*, 2008, **319**, 939.

103 D.-X. Xue, Y. Belmabkhout, O. Shekhah, H. Jiang, K. Adil, A. J. Cairns and M. Eddaoudi, *J. Am. Chem. Soc.*, 2015, **137**, 5034.

104 D. K. Singha, P. Majee, S. Mandal, S. K. Mondal and P. Mahata, *Inorg. Chem.*, 2018, **57**, 12155.

105 D. K. Singha, P. Majee, S. Hui, S. K. Mondal and P. Mahata, *Dalton Trans.*, 2020, **49**, 829.

106 P. Daga, S. Sarkar, P. Majee, D. K. Singha, S. Hui, P. Mahata and S. K. Mondal, *Mater. Adv.*, 2021, **2**, 985.

107 P. Majee, P. Daga, D. K. Singha, D. Saha, P. Mahata and S. K. Mondal, *J. Photochem. Photobiol., A*, 2020, **402**, 112830.

108 Y. Ban, Y. Li, X. Liu, Y. Peng and W. Yang, *Microporous Mesoporous Mater.*, 2013, **173**, 29.

109 N. Stock and S. Biswas, *Chem. Rev.*, 2012, **112**, 933.

110 P. Majee, D. K. Singha, P. Daga, S. Hui, P. Mahata and S. K. Mondal, *CrystEngComm*, 2021, **23**, 4160.

111 S. Henke, A. Schneemann, S. Kapoor, R. Winter and R. A. Fischer, *J. Mater. Chem.*, 2012, **22**, 909.

112 Y. Sun and H.-C. Zhou, *Sci. Technol. Adv. Mater.*, 2015, **16**, 054202.

113 M. Klimakow, P. Klobes, A. F. Thünemann, K. Rademann and F. Emmerling, *Chem. Mater.*, 2010, **22**, 5216.

114 B. Szczęśniak, S. Borysiuk, J. Choma and M. Jaroniec, *Mater. Horiz.*, 2020, **7**, 1457.

115 N. K. Singh, M. Hardi and V. P. Balema, *Chem. Commun.*, 2013, **49**, 972.

116 D. Chen, J. Zhao, P. Zhang and S. Dai, *Polyhedron*, 2019, **162**, 59.

117 A. Martinez Joaristi, J. Juan-Alcañiz, P. Serra-Crespo, F. Kapteijn and J. Gascon, *Cryst. Growth Des.*, 2012, **12**, 3489.

118 S. Khazalpour, V. Safarifard, A. Morsali and D. Nematollahi, *RSC Adv.*, 2015, **5**, 36547.

119 H. Ren and T. Wei, *ChemElectroChem*, 2022, **9**, e202200196.

120 H. Al-Kutubi, J. Gascon, E. J. R. Sudhölter and L. Rassaei, *ChemElectroChem*, 2015, **2**, 462.

121 W.-J. Son, J. Kim, J. Kim and W.-S. Ahn, *Chem. Commun.*, 2008, 6336, DOI: **10.1039/B814740J**.

122 K. Yu, Y.-R. Lee, J. Y. Seo, K.-Y. Baek, Y.-M. Chung and W.-S. Ahn, *Microporous Mesoporous Mater.*, 2021, **316**, 110985.

123 T. Wiwasuku, J. Othong, J. Boonmak, V. Ervithayasuporn and S. Youngme, *Dalton Trans.*, 2020, **49**, 10240.

124 J. H. Lee, Y. Ahn and S.-Y. Kwak, *ACS Omega*, 2022, **7**, 23213.

125 J. Klinowski, F. A. Almeida Paz, P. Silva and J. Rocha, *Dalton Trans.*, 2011, **40**, 321.

126 M. Taddei, P. V. Dau, S. M. Cohen, M. Ranocchiari, J. A. van Bokhoven, F. Costantino, S. Sabatini and R. Vivani, *Dalton Trans.*, 2015, **44**, 14019.

127 R. Babu, R. Roshan, A. C. Kathalikkattil, D. W. Kim and D.-W. Park, *ACS Appl. Mater. Interfaces*, 2016, **8**, 33723.

128 Z.-J. Lin, Z. Yang, T.-F. Liu, Y.-B. Huang and R. Cao, *Inorg. Chem.*, 2012, **51**, 1813.

129 S. Parshamoni and S. Konar, *CrystEngComm*, 2016, **18**, 4395.

130 K. Tomar, R. Rajak, S. Sanda and S. Konar, *Cryst. Growth Des.*, 2015, **15**, 2732.

131 A. Halder, A. Maiti, S. Dinda, B. Bhattacharya and D. Ghoshal, *Cryst. Growth Des.*, 2021, **21**, 6110.

132 G. Pahari, S. Ghosh, A. Halder and D. Ghoshal, *Cryst. Growth Des.*, 2021, **21**, 2633.

133 P. Daga, P. Manna, P. Majee, D. K. Singha, S. Hui, A. K. Ghosh, P. Mahata and S. K. Mondal, *Dalton Trans.*, 2021, **50**, 7388.

134 C. Petit and T. J. Bandosz, *Adv. Mater.*, 2009, **21**, 4753.

135 K. Jayaramulu, K. K. R. Datta, C. Rösler, M. Petr, M. Otyepka, R. Zboril and R. A. Fischer, *Angew. Chem., Int. Ed.*, 2016, **55**, 1178.

136 Y. Chen, Y. Xie, S. A. Yang, H. Pan, F. Zhang, M. L. Cohen and S. Zhang, *Nano Lett.*, 2015, **15**, 6974.

137 Y. Fu, J. Zhang, H. Liu, W. C. Hiscox and Y. Gu, *J. Mater. Chem. A*, 2013, **1**, 2663.

138 D. R. Dreyer, H.-P. Jia and C. W. Bielawski, *Angew. Chem., Int. Ed.*, 2010, **49**, 6813.

139 P. Kumar, G. Singh, D. Tripathi and S. L. Jain, *RSC Adv.*, 2014, **4**, 50331.

140 M. Mahyari and A. Shaabani, *Appl. Catal., A*, 2014, **469**, 524.

141 S. Sundriyal, V. Shrivastav, H. Kaur, S. Mishra and A. Deep, *ACS Omega*, 2018, **3**, 17348.

142 W. Cao, M. Han, L. Qin, Q. Jiang, J. Xu, Z. Lu and Y. Wang, *J. Solid State Electrochem.*, 2019, **23**, 325.

143 M. Azadfalah, A. Sedghi, H. Hosseini and H. Kashani, *J. Energy Storage*, 2021, **33**, 101925.

144 N. S. Punde, C. R. Rawool, A. S. Rajpurohit, S. P. Karna and A. K. Srivastava, *ChemistrySelect*, 2018, **3**, 11368.

145 M. Azadfalah, A. Sedghi and H. Hosseini, *J. Mater. Sci.: Mater. Electron.*, 2019, **30**, 12351.

146 Y. Zhong, X. Cao, L. Ying, L. Cui, C. Barrow, W. Yang and J. Liu, *J. Colloid Interface Sci.*, 2020, **561**, 265.

147 Y. Xiao, W. Wei, M. Zhang, S. Jiao, Y. Shi and S. Ding, *ACS Appl. Energy Mater.*, 2019, **2**, 2169.

148 J. Kim, S.-J. Park, S. Chung and S. Kim, *J. Nanosci. Nanotechnol.*, 2020, **20**, 2750.

149 F. He, N. Yang, K. Li, X. Wang, S. Cong, L. Zhang, S. Xiong and A. Zhou, *J. Mater. Res.*, 2020, **35**, 1439.

150 R. Sahoo, S. Ghosh, S. Chand, S. Chand Pal, T. Kuila and M. C. Das, *Composites, Part B*, 2022, **245**, 110174.

151 T. Chen, T. Shen, Y. Wang, Z. Yu, W. Zhang, Y. Zhang, Z. Ouyang, Q. Cai, Y. Ji and S. Wang, *ACS Omega*, 2023, **8**, 10888.

152 S. Qiang Zheng, S. Shee Lim, C. Yi Foo, C. Yian Haw, W. Siong Chiu, C. Hua Chia and P. Sim Khiew, *J. Electroanal. Chem.*, 2022, **925**, 116860.

153 M. Azadfalah, A. Sedghi and H. Hosseini, *J. Electron. Mater.*, 2019, **48**, 7011.

154 M. K. Singh, A. K. Gupta, S. Krishnan, N. Guha, S. Marimuthu and D. K. Rai, *J. Energy Storage*, 2021, **43**, 103301.

155 Y. Ehrnst, H. Ahmed, R. Komljenovic, E. Massahud, N. A. Shepelin, P. C. Sherrell, A. V. Ellis, A. R. Rezk and L. Y. Yeo, *J. Mater. Chem. A*, 2022, **10**, 7058.

156 D. Mohanadas, M. A. A. Mohd Abdah, N. H. N. Azman, J. Abdullah and Y. Sulaiman, *Int. J. Hydrogen Energy*, 2021, **46**, 35385.

157 S. Krishnan, A. K. Gupta, M. K. Singh, N. Guha and D. K. Rai, *Chem. Eng. J.*, 2022, **435**, 135042.

158 P. Srimuk, S. Luanwuthi, A. Krittayavathananon and M. Sawangphruk, *Electrochim. Acta*, 2015, **157**, 69.

159 L. Liu, Y. Yan, Z. Cai, S. Lin and X. Hu, *Adv. Mater. Interfaces*, 2018, **5**, 1701548.

160 Q. V. Thi, S. A. Patil, P. K. Katkar, I. Rabani, A. S. Patil, J. Ryu, G. Kolekar, N. T. Tung and D. Sohn, *Synth. Met.*, 2022, **290**, 117155.

161 W. Zhang, Y. Tan, Y. Gao, J. Wu, J. Hu, A. Stein and B. Tang, *J. Appl. Electrochem.*, 2016, **46**, 441.

162 K. Jayaramulu, M. Horn, A. Schneemann, H. Saini, A. Bakandritsos, V. Ranc, M. Petr, V. Stavila, C. Narayana, B. Scheibe, Š. Kment, M. Otyepka, N. Motta, D. Dubal, R. Zbořil and R. A. Fischer, *Adv. Mater.*, 2021, **33**, 2004560.

163 M. Majumder, R. B. Choudhary, A. K. Thakur, A. Khodayari, M. Amiri, R. Boukherroub and S. Szunerits, *Electrochim. Acta*, 2020, **353**, 136609.

164 S. A. Hira and K. H. Park, *ACS Appl. Nano Mater.*, 2021, **4**, 7870.

165 P. C. Banerjee, D. E. Lobo, R. Middag, W. K. Ng, M. E. Shaibani and M. Majumder, *ACS Appl. Mater. Interfaces*, 2015, **7**, 3655.

166 A. Farisabadi, M. Moradi, S. Borhani, S. Hajati, M. A. Kiani and S. A. Tayebifard, *J. Mater. Sci.: Mater. Electron.*, 2018, **29**, 8421.

167 L. G. Beka, X. Bu, X. Li, X. Wang, C. Han and W. Liu, *RSC Adv.*, 2019, **9**, 36123.

168 J. Hong, S.-J. Park and S. Kim, *Electrochim. Acta*, 2019, **311**, 62.

169 Z. Andikaey, A. A. Ensafi and B. Rezaei, *Int. J. Hydrogen Energy*, 2020, **45**, 32059.

170 M. S. Rahmanifar, H. Hesari, A. Noori, M. Y. Masoomi, A. Morsali and M. F. Mousavi, *Electrochim. Acta*, 2018, **275**, 76.

171 S. Kumaraguru, J. Yesuraj and S. Mohan, *Composites, Part B*, 2020, **185**, 107767.

172 C. Shi, H. Cao, S. Li, L. Guo, Y. Wang and J. Yang, *J. Energy Storage*, 2022, **54**, 105270.

173 M. Safari and J. Mazloom, *J. Energy Storage*, 2023, **58**, 106390.

174 E. Erçarıkcı, K. Dağcı Kıranşan and E. Topçu, *Energy Fuels*, 2022, **36**, 1735.

175 A. S. Rajpurohit, N. S. Punde and A. K. Srivastava, *J. Colloid Interface Sci.*, 2019, **553**, 328.

176 S. Sundriyal, H. Kaur, S. K. Bhardwaj, S. Mishra, K.-H. Kim and A. Deep, *Coord. Chem. Rev.*, 2018, **369**, 15.

177 H. Yang, G.-X. Zhang, H.-J. Zhou, Y.-Y. Sun and H. Pang, *Energy Mater. Adv.*, 2023, **4**, 0033.

178 S. Zheng, H. Zhou, H. Xue, P. Braunstein and H. Pang, *J. Colloid Interface Sci.*, 2022, **614**, 130.

179 H. Zhang, Z. Li, Z. Hou, H. Mei, Y. Feng, B. Xu and D. Sun, *Chem. Eng. J.*, 2021, **425**, 130602.

180 L. Luo, Y. Zhou, W. Yan, G. Du, M. Fan and W. Zhao, *J. Colloid Interface Sci.*, 2022, **615**, 282.

181 Z. Cao, R. Momen, S. Tao, D. Xiong, Z. Song, X. Xiao, W. Deng, H. Hou, S. Yasar, S. Altin, F. Bulut, G. Zou and X. Ji, *Nano-Micro Lett.*, 2022, **14**, 181.

182 P. Wen, P. Gong, J. Sun, J. Wang and S. Yang, *J. Mater. Chem. A*, 2015, **3**, 13874.

183 Z. Neisi, Z. Ansari-Asl and A. S. Dezfuli, *J. Inorg. Organomet. Polym. Mater.*, 2019, **29**, 1838.

184 Z. Li, Y. Tan, W. Zhang and B. Tang, *Ionics*, 2016, **22**, 2545.

185 S. Yao, Y. Jiao, S. Sun, L. Wang, P. Li and G. Chen, *ACS Sustainable Chem. Eng.*, 2020, **8**, 3191.

186 R. Patil, L. Pradhan, B. M. Matsagar, O. Agrawal, K. C. W. Wu, B. K. Jena and S. Dutta, *Energy Adv.*, 2023, DOI: **10.1039/d3ya00206c**.

187 R. I. Mohanty, A. Mukherjee, P. Bhanja and B. K. Jena, *J. Energy Storage*, 2023, **72**, 108730.

188 B. Mohanty, L. Pradhan, M. Kandasamy, B. Chakraborty and B. K. Jena, *Energy Fuels*, 2023, **37**, 7530.